
# NAVAL POSTGRADUATE SCHOOL

**MONTEREY, CALIFORNIA**

# THESIS

**DEVELOPMENT OF A 2-DEGREE-OF-FREEDOM TRANSVERSE LINE SOURCE FOR A SEISMO-ACOUSTIC SONAR**

by

Wang, Shu-Kang

December 2005

Thesis Advisor: Steven R. Baker

**Approved for public release; distribution is unlimited.**

THIS PAGE INTENTIONALLY LEFT BLANK

| REPORT DOCUMENTATION PAGE | | | Form Approved OMB No. 0704-0188 |
|---|---|---|---|
| Public reporting burden for this collection of information is estimated to average 1 hour per response, including the time for reviewing instruction, searching existing data sources, gathering and maintaining the data needed, and completing and reviewing the collection of information. Send comments regarding this burden estimate or any other aspect of this collection of information, including suggestions for reducing this burden, to Washington headquarters Services, Directorate for Information Operations and Reports, 1215 Jefferson Davis Highway, Suite 1204, Arlington, VA 22202-4302, and to the Office of Management and Budget, Paperwork Reduction Project (0704-0188) Washington DC 20503. | | | |
| **1. AGENCY USE ONLY *(Leave blank)*** | **2. REPORT DATE** December 2005 | **3. REPORT TYPE AND DATES COVERED** Master's Thesis | |
| **4. TITLE AND SUBTITLE**: Development of a 2-Degree-of-Freedom Transverse Line Source for a Seismo-Acoustic SONAR | | **5. FUNDING NUMBERS** | |
| **6. AUTHOR(S) Wang, Shu-Kang** | | | |
| **7. PERFORMING ORGANIZATION NAME(S) AND ADDRESS(ES)** Naval Postgraduate School Monterey, CA 93943-5000 | | **8. PERFORMING ORGANIZATION REPORT NUMBER** | |
| **9. SPONSORING /MONITORING AGENCY NAME(S) AND ADDRESS(ES)** N/A | | **10. SPONSORING/MONITORING AGENCY REPORT NUMBER** | |
| **11. SUPPLEMENTARY NOTES** The views expressed in this thesis are those of the author and do not reflect the official policy or position of the Department of Defense or the U.S. Government. | | | |
| **12a. DISTRIBUTION / AVAILABILITY STATEMENT** Approved for public release; distribution is unlimited | | **12b. DISTRIBUTION CODE** | |


**13. ABSTRACT (maximum 200 words)**

This thesis describes the beach field-testing of a 2-degree-of-freedom (2-DOF) transverse line Rayleigh wave source for use in a seismo-acoustic SONAR for buried mine detection. The source is composed of six identical modules, each composed of two radial and two vertical inertial mass shakers, all mounted to a common base plate. The vertical and horizontal excitation of each module is independent. Electrically, the six modules are organized into three independent sets of two. The length of the source is 46 inches (1.17m), the width 6 inches (0.15m) and the weight 126 pounds (562N). Field tests were conducted using a 5-cycle, (smooth-)amplitude-modulated transient excitation signal. Based on past and present experience that the Rayleigh wave speed at the beach test site is approximately 90 m/s, a carrier frequency of 100 Hz was employed, producing a Rayleigh wavelength and surface penetration depth of approximately 1 m (approximately equal to the source aperture length), which is appropriate for the intended application. The source radiation directional characteristics were investigated for various relative amplitudes and phases of vertical and horizontal shaker excitation. A null result was obtained, that is, no unambiguous evidence of directivity was observed in any of the experiments conducted using this source. These included measurements wherein the source modules were removed from the common base plate and emplaced on the sand. The reason for this result is unknown, but it is suspected that a good possibility is that the beach sand medium just below its surface, whereupon the present source and receivers were deployed, is not homogeneous enough to support coherent spatial beamforming. Based upon the past success of a 4-element end-fire line array in producing directional Rayleigh wave radiation (10-15 dB front-to-back rejection), it is suggested that, if such a source can be made mobile, it may well be the best source candidate for a seismo-acoustic SONAR for buried mine detection.


| **14. SUBJECT TERMS** Seismic-Acoustic, 2-DOF transverse line source, Rayleigh wave | | | **15. NUMBER OF PAGES** 107 |
|---|---|---|---|
| | | | **16. PRICE CODE** |
| **17. SECURITY CLASSIFICATION OF REPORT** Unclassified | **18. SECURITY CLASSIFICATION OF THIS PAGE** Unclassified | **19. SECURITY CLASSIFICATION OF ABSTRACT** Unclassified | **20. LIMITATION OF ABSTRACT** UL |

NSN 7540-01-280-5500

Standard Form 298 (Rev. 2-89)
Prescribed by ANSI Std. 239-18

THIS PAGE INTENTIONALLY LEFT BLANK

**Approved for public release; distribution is unlimited.**

# DEVELOPMENT OF A 2-DOF TRANSVERSE LINE SOURCE FOR A SEISMO-ACOUSTIC SONAR

Wang, Shu-Kang
Lieutenant, ROC, Taiwan Navy
B.E.E., Chinese Naval Academy, 1998

Submitted in partial fulfillment of the
requirements for the degrees of

**MASTER OF SCIENCE IN APPLIED PHYSICS**

from the

**NAVAL POSTGRADUATE SCHOOL**
**December 2005**

Author: Wang, Shu-Kang

Approved by: Steven R. Baker
Thesis Advisor

James Luscombe
Chairman
Department of Physics

THIS PAGE INTENTIONALLY LEFT BLANK

# ABSTRACT

This thesis describes the beach field-testing of a 2-degree-of-freedom (2-DOF) transverse line Rayleigh wave source for use in a seismo-acoustic SONAR for buried mine detection. The source is composed of six identical modules, each composed of two vertical and two horizontal inertial mass shakers, all mounted to a common base plate. The vertical and horizontal excitation of each module is independent. Electrically, the six modules are organized into three independent sets of two. The length of the source is 46 inches (1.17m), the width 6 inches (0.15m) and the weight 126 pounds (562N). Field tests were conducted using a 5-cycle, (smooth-)amplitude-modulated transient excitation signal. Based on past and present experience that the Rayleigh wave speed at the beach test site is approximately 90 m/s, a carrier frequency of 100 Hz was employed, producing a Rayleigh wavelength and surface penetration depth of approximately 1 m (approximately equal to the source aperture length), which is appropriate for the intended application. The source radiation directional characteristics were investigated for various relative amplitudes and phases of vertical and horizontal shaker excitation. A null result was obtained, that is, no unambiguous evidence of directivity was observed in any of the experiments conducted using this source. These included measurements wherein the source modules were removed from the common base plate and emplaced on the sand. The reason for this result is unknown, but it is suspected that a good possibility is that the beach sand medium just below its surface, whereupon the present source and receivers were deployed, is not homogeneous enough to support coherent spatial beamforming. Based upon the past success of a 4-element end-fire line array in producing directional Rayleigh wave radiation (10-15 dB front-to-back rejection), it is suggested that, if such a source can be made mobile, it may well be the best source candidate for a seismo-acoustic SONAR for buried mine detection.

THIS PAGE INTENTIONALLY LEFT BLANK

# TABLE OF CONTENTS

# LIST OF FIGURES

# LIST OF TABLES

THIS PAGE INTENTIONALLY LEFT BLANK

# ACKNOWLEDGMENTS

I feel an immense gratitude to my thesis advisor Professor Steve Baker for his enthusiasm and patience. I also owe him an apology as I am not a native English speaker, which often requires that he repeat what he has said to me many times before I understand. Thanks also go to Sam Barone and George Jaksha for their electrical and mechanical expertise in maintaining the apparatus in good condition.

THIS PAGE INTENTIONALLY LEFT BLANK

# I. INTRODUCTION

Buried landmines and ordnance are effective weapons in preventing military forces from projecting power into an area and limiting military operations. The first modern, high explosive, anti-personnel (AP) landmine was produced in Germany in 1912, and was copied and manufactured by other major countries in War World I. [Ref. 1]

## A. THE LANDMINE PROBLEM

Countries have made widespread use of landmines in internal and international conflicts around the world. The massive use of landmines in recent decades has resulted in a great number of injuries and deaths – both military and civilian. Landmines are often buried without any record of their locations, making them difficult to find and remove. According to the International Red Cross record, even though the military conflicts have stopped, these landmines are still injuring or killing an average of 2000 people per month, mainly civilians and children. There are an estimated 130 million landmines buried in the ground in at least 70 countries in Africa, Asia, Europe, the Middle East, and the Americas; the number of newly buried landmines increases at a rate of 2 million per year. Once the landmines are buried, they can remain active for an average of 50 years. It costs between $3 and $30 to produce a landmine, but the average cost to remove one is approximately $300 to $1000. Surgical care and prosthetics amounts to $4000 per amputee. [Ref. 2] The United Nations estimates that it would take over 1,000 years with a cost of approximately $33 billion to safely remove the landmines buried all over the world by conventional methods. [Ref. 3]

With an increased focus on world peace and humanitarianism, mine sweeping has become an important international issue and a priority for many countries. Cambodia is a country with a population of ten million, but also a home to millions of landmines. The number of buried mines in Cambodia is greater than the number of children, by a factor of two to one. [Ref. 4] In Korea, at least

one million landmines are buried in the Demilitarized Zone that divides North Korea and South Korea. [Ref. 5] With the assistance of the United States, over 300,000 landmines buried by Iraq in Kuwait during the Gulf War have been cleared out, making Kuwait the first country to be cleared of landmines. [Ref. 3] Another example is that, since 1949, an estimated 300,000 landmines have been buried on Jin Men, Taiwan, an island with an area of $150\,km^2$, which is roughly 18 miles from Mainland China, to prevent the Liberation Army from landing a military operation there. [Ref. 6] The Taiwanese authority is making an effort to clear these mines in order to provide a clean and safe land to the inhabitants in Jin Men. While efforts to ban the use and manufacture of the landmines are beneficial, more effective technologies must be developed to detect and remove buried mines more quickly and safely.

Landmines are cheap and easy to manufacture, but expensive to locate and remove. Modern landmines are small, made of plastic, and contain very little metal, thereby increasing the difficulty in detecting them. A number of technical methods used for buried mine detection have been developed and this research will focus on the application of seismo-acoustic surface (Rayleigh) waves. Due to the different mechanical and elastic properties between mines and the surrounding earth, seismo-acoustic techniques have been considered as effective methods of mine detection. When a Rayleigh wave propagates through a region containing a mine, it causes different displacements of the mine versus the surrounding earth, resulting in scattered radiation (an echo). Receivers can be used to detect this scattered radiation in order to locate the mines. The research reported herein is concerned with the development of a directional source of Rayleigh waves for use in a seismo-acoustic SONAR for the detection of buried mines.

This thesis contains six chapters. The introduction describes the research motivation and objective for the present investigation. The second chapter contains a general overview of seismic waves and the reasons that make Rayleigh waves a good choice to detect buried ordnance. The third chapter

relates the previous work related to this research. The fourth chapter details the equipment that was used to test the source on the sand beach. The fifth chapter is the major part of this research and describes the experiment results. The last chapter provides the conclusion.

## B. RESEARCH MOTIVATION

In order to minimize the number of casualties due to mine sweeping, safer and more efficient methods have been developed. The concept of a seismo-acoustic SONAR for detecting buried ordnance was introduced in the early 1990s and was investigated by Prof. Thomas Muir and his colleagues at the Applied Research Laboratory of the University of the Texas at Austin. [Ref. 7] Figure 1 shows the concept of the seismo-acoustic SONAR using Rayleigh waves, which are guided surface elastic waves. Rayleigh waves propagate through the ground, scattering off of buried objects. The scattered waves are then received by the sensors to determine the locations of the objects.

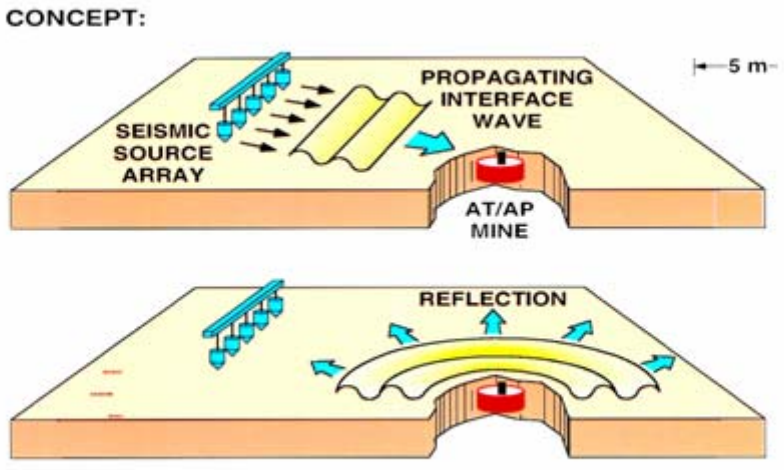


Figure 1. Seismo-Acoustic SONAR Concept

## C. RESEARCH OBJECTIVE

The focus of this research is on source development. The major challenges in the development of an optimum seismo-acoustic SONAR source are to :

- Mobilize sources while maintaining good ground coupling to the earth.
- Develop unidirectional sources.
- Suppress body waves

Research by previous NPS students has included the investigation of several candidate mobile sources. These are discussed later in comparison with the results of the present investigation.

The objective of the present research was to investigate the effectiveness of a candidate 2-degree-of-freedom line source for use in the seismo-acoustic SONAR. Source radiation measurements were taken on a sand beach, utilizing various configurations and ranges and angular positions of the receivers and different frequencies and phases to excite independent radial and vertical ground motion. These measurements were used to determine the Rayleigh wave propagation speed and far-field beam patterns.

# II. SEISMIC WAVES

When a stress is rapidly applied to an elastic medium and causes displacement or distortion at a point, an elastic wave is radiated and propagates through the medium. When the medium is the Earth, such waves are termed seismic waves or seismo-acoustic waves.

There are two types of elastic waves, body waves and surface waves. Because surface waves are confined to near the surface of a medium, they propagate in a cylindrical fashion. Body waves travel throughout the medium, which is in three dimensions. These waves propagate in a spherical fashion. The amplitude of surface waves decays exponentially into the medium and also inversely proportional to the square root of the distance; the amplitude of body waves is inversely proportional to the distance from the source. Therefore, surface waves decay more slowly with distance than body waves. The sections below will give a brief introduction to body waves and surface waves. [Ref. 10]

In this thesis, it is assumed that the sand beach area where the experiment was done is a homogeneous and elastic medium, i.e., the beach is uniform and all the points along the beach have the same properties. When surface waves propagate in this beach area and apply forces on sand particles, these particles oscillate. They return back to their initial positions when the forces disappear. In reality, the properties of the beach can be affected by the tide and certainly vary with depth and water saturation, so it is not a uniform and homogenous medium for wave propagation.

## A. BODY WAVES

There are two types of body waves, P-waves (primary waves) and S-waves (secondary waves), classified by their motion property. P-waves are longitudinal waves, or compression waves, and are the fastest seismic waves; the direction of wave propagation is same as the motion of the particles. P-waves can propagate through solid and fluid media with speed given by

$$V_p = \sqrt{\frac{k + 4\mu/3}{\rho}},$$

where $k$ is the bulk modulus, $\mu$ is the shear modulus, and $\rho$ is the density of the medium. Figure 2 shows the propagation of a P-wave.

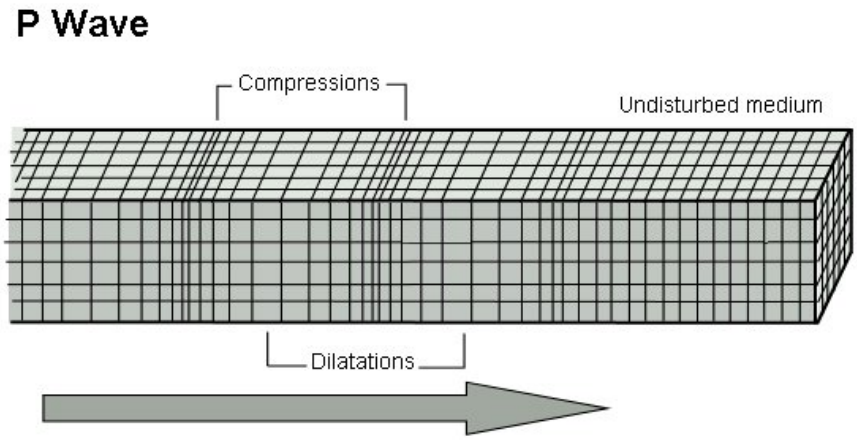


Figure 2. Propagation of P Waves

S-waves are shear waves, or transverse waves, with wave speed slower than a P-wave, and the direction of wave propagation is perpendicular to the motion of the particles. Since liquids do not posses the property shear elasticity, S-waves can not propagate through liquid media. Shear waves can be polarized into vertical and horizontal orientations, which are called SV (shear-vertical) waves and SH (shear-horizontal) waves. The speed of an S-wave is given by

$$V_s = \sqrt{\frac{\mu}{\rho}},$$

where, again, $\mu$ is the shear modulus, and $\rho$ is the density of the medium. Figure 3 shows the propagation of an S-wave.

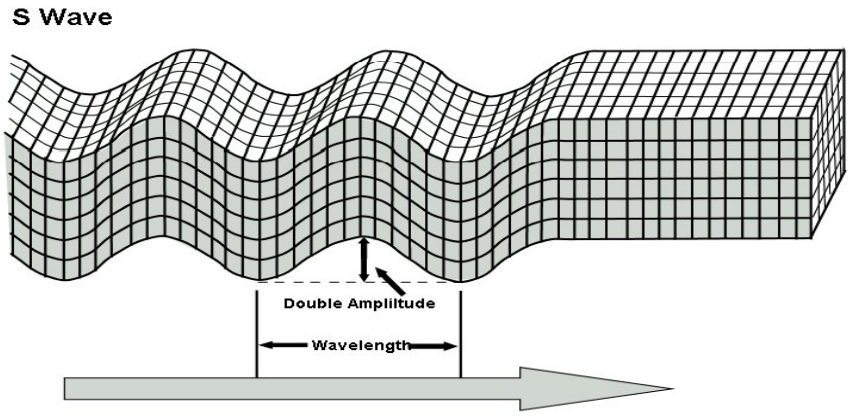


Figure 3. Propagation of S Waves

The speed of both P-waves and S-waves is affected by temperature and pressure, decreasing with temperature and increasing with pressure. [Ref. 10]

## B. SURFACE WAVES

Assuming that the medium is infinite and homogeneous, P-waves and S-waves spherically propagate independently through the medium. When they encounter a boundary or an interface with a different medium, these two waves are mixed together and create surface waves. Surface waves propagate along the surface of the earth with larger amplitude and longer duration and with propagation speed slower than body waves.

There are two types of surface seismic waves, Love waves and Rayleigh waves. Love waves (also called Q waves) were found by English physicist A. E. H. Love in 1911, who used mathematical methods to predict their existence. Love waves propagate transversely, with no vertical particle motion. They are formed by the reflections of SH waves and propagate in a duct between two boundaries; they do not exist in a homogeneous half-space. Love waves have a cutoff frequency and are dispersive. The speed of Love waves is slower than the P- or S- waves, but faster than Rayleigh waves. Figure 4 shows the propagation of Love waves.

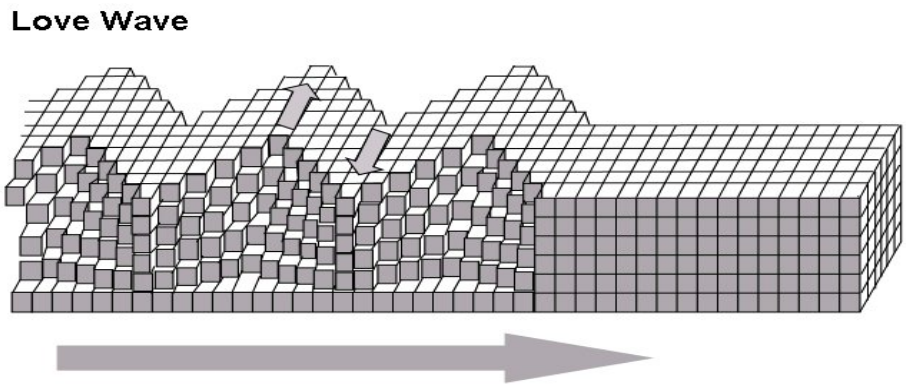


Figure 4. Propagation of Love Waves

Rayleigh waves, which posses both longitudinal and transverse particle motion, were found by Lord Rayleigh in 1885. They are nondispersive and have zero cutoff frequency. A Rayleigh wave is like an ocean wave, in that the particle motion is elliptical, except that in the ocean wave the motion is prograde while for Rayleigh waves it is retrograde at the surface. Figure 5 shows that Rayleigh waves are created by the interaction of P-waves and SV waves at the surface, which is taken to be stress free.

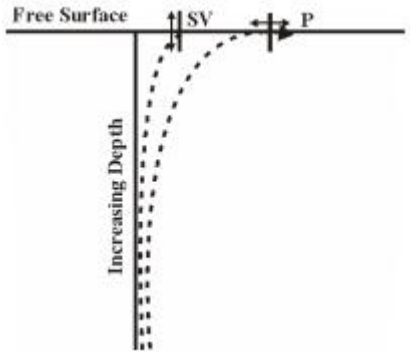


Figure 5. Interaction of P-Waves and SV Waves at the Surface

Rayleigh waves propagate with retrograde elliptical particle motion at the surface and in a vertical plane parallel to the direction of the wave propagation. Figure 6 shows the propagation of Rayleigh waves. The long axis of this elliptical

particle path is perpendicular to the surface, while the short axis of this elliptical particle path is parallel to the direction of wave propagation, i.e. radial. The ratio of the length of the long axis to the short axis depends upon the elastic moduli. A typical value is 1.5.

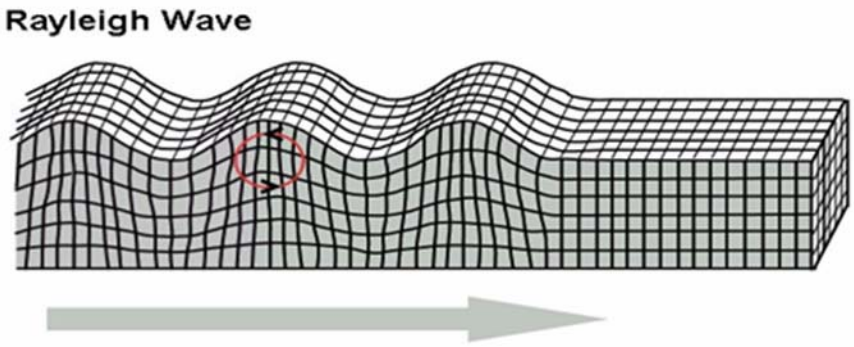


Figure 6. Propagation of a Rayleigh Wave

In Rayleigh waves, particles at the surface move in a retrograde elliptical motion. Particles with a depth larger than about one-fifth of the wavelength of the Rayleigh wave move in a prograde elliptical motion. In prograde elliptical motion, the vertical motion leads the outward radial motion by 90 degrees, whereas, in retrograde elliptical motion, the outward radial motion leads the vertical motion by 90 degrees. Figure 7 shows the two types of Rayleigh wave motion.

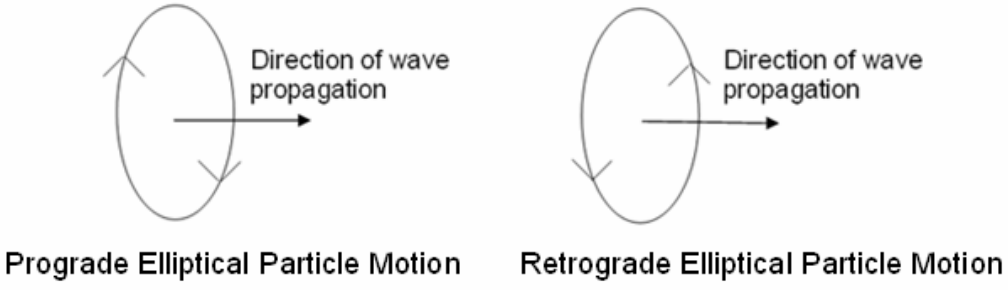


Figure 7. Prograde and Retrograde Elliptical Particle Motion

If a plane wave propagates through an elastic medium with stress free boundary conditions, then the wave equations can be written as

$$\frac{\partial^2 \phi}{\partial t^2} = c_l{}^2 \nabla^2 \phi \,,$$

$$\frac{\partial^2 \psi}{\partial t^2} = c_s{}^2 \nabla^2 \psi \,,$$

where $\phi$ and $\psi$ represent the compression and rotation in the medium, respectively, $c_l$ is the longitudinal wave speed, and $c_s$ is the shear wave speed. [Ref. 10]

The Rayleigh wave propagation speed is given by

$$c_r = c_s \kappa \,,$$

where $c_r$ is the Rayleigh wave speed, and $\kappa$ is the ratio of Rayleigh wave speed to the shear wave speed, and is a dimensionless parameter, given by the real-valued roots of the bicubic equation,

$$\kappa^6 - 8\kappa^4 + (24 - 16\gamma^2)\kappa^2 + (16\gamma^2 - 16) = 0 \,.$$

This is the Rayleigh equation. In general, the Rayleigh wave speed is approximately 90 percent of the shear wave speed, that is to say, $\kappa$ is about 0.9. Typical Rayleigh wave speed values observed at the beach test site range from approximately 85m/s to 105m/s. $\gamma$ is the ratio of the shear wave speed to the longitudinal wave speed and is given by

$$\gamma^2 = (\frac{c_s}{c_l})^2 = \frac{\mu}{\lambda + 2\mu} = \frac{1 - 2\nu}{2 - 2\nu},$$

where $c_s$ is the shear wave speed, $c_l$ is the longitudinal wave speed, $\lambda$ and $\mu$ are the Lame constants, and $\nu$ is Poisson's Ratio. The solution of the Rayleigh wave equation is a real and positive root in the interval $\kappa^2 = (0, 1)$, corresponding to the value of Poisson's Ratio in the interval $\nu = (0, 0.5)$.

The Rayleigh wave speed is the slowest compared to other types of seismic waves. The amplitude of Rayleigh waves decreases exponentially with depth. Figure 8 shows the motion of particles in Rayleigh waves with depth.

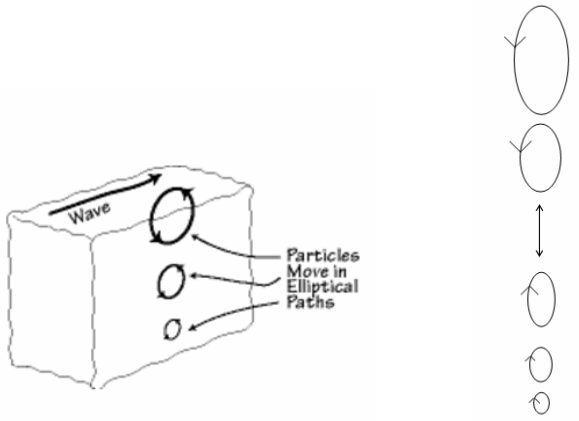


Figure 8. The Amplitude of Rayleigh Waves Decreases Exponentially with Depth

Figure 9 shows a graph of particle motion as a function of depth. At the depth h, the horizontal motion is zero and results in only vertical motion. At depths greater than h, the direction of particle rotation changes from retrograde to prograde, that is to say, the particle motion is retrograde elliptical above depth h and prograde elliptical at depths deeper than h. The value of h is approximately equal to $0.1\lambda_R$ for real sediments, approximately $0.2\lambda_R$ for solids, where $\lambda_R$ is the Rayleigh wavelength. [Ref. 8] Near the surface, radial wave motion (U) decays more rapidly than the vertical (V) wave motion; both of them have the same decay constant below a certain depth.

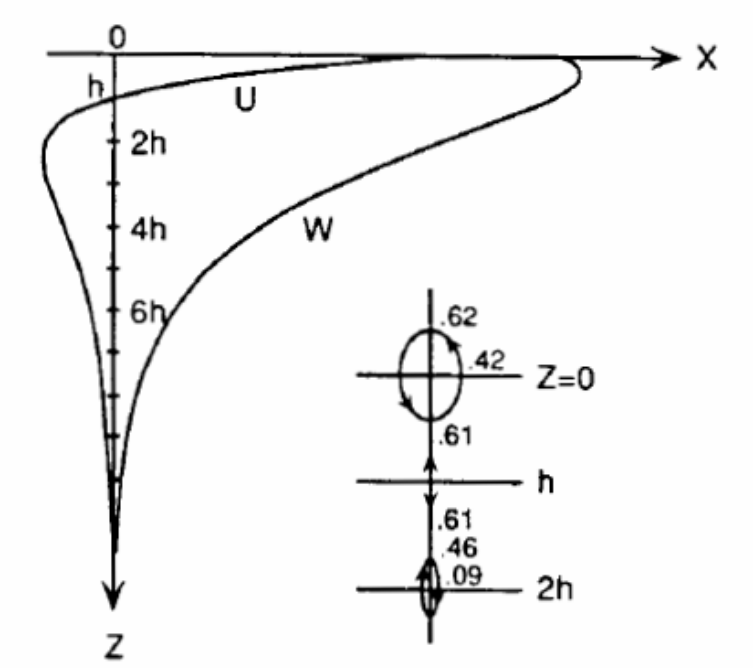


Figure 9. The horizontal (U) and the vertical (W) displacement for Rayleigh waves in a homogeneous half-space. U vanishes at depth h. The path of the particles is elliptic retrograde for z<h and elliptic direct (prograde) for z>h. [Ref. 9]

In general, the amplitude of body waves decays more quickly with range than that of surface waves. Also, reflected waves can be created when body waves interact with an interface boundary. For these two reasons, body waves are not the proper type to use in detecting buried landmines. These reflected waves will be received by sensors and result in difficulties in distinguishing waves scattered from a buried mine-like object. [Ref. 10] Since the amplitude of the Rayleigh waves decrease proportional to $1/\sqrt{r}$, where r is the distance from the source, Rayleigh waves carry more seismic wave energy than shear waves and compression waves. Rayleigh waves carry about 67% of the seismic wave energy at the surface, shear waves 26% and compression waves 7%. [Ref. 8] And, as mentioned before, they are nondispersive and have zero cutoff frequency. These features make Rayleigh waves a suitable choice for a seismo-acoustic SONAR source.

## C. DESIRABLE PROPERTIES OF RAYLEIGH WAVES FOR USE IN A SEISMO-ACOUSTIC SONAR FOR BURIED MINE DETECTION

- Ideal Rayleigh waves are non-dispersive (in a homogeneous, isotropic medium), which means the phase velocity is independent of frequency, and have zero cutoff frequency. (unlike Love waves)
- The particle motion is within approximately two wavelengths of depth. (suppressing strong reflections from layers)
- Rayleigh waves are easy to produce and the particle motion is a retrograde elliptical path at the surface. (which provides some discrimination from body waves)

In reality, all surface waves are dispersive and the depth that Rayleigh waves can penetrate depends on frequency. Shear modulus increases with increasing depth and the shear velocity increases with depth, also. Therefore, dispersion should be taken into account. A higher frequency Rayleigh wave propagates more slowly than one at a lower frequency. This is because a lower frequency Rayleigh wave has a longer wavelength. Long wavelength waves penetrate more deeply into the Earth than short wavelength waves. Since the shear velocity in the Earth increases with increasing depth, the longer wavelength, or low frequency, waves can propagate faster than the shorter wavelength, or high frequency, waves. This complication is not addressed herein.

THIS PAGE INTENTIONALLY LEFT BLANK

# III. PREVIOUS RESEARCH

The concept of a seismo-acoustic SONAR for buried mine and ordnance detection using Rayleigh waves was investigated by Dr. Thomas G. Muir when he worked at the Applied Research Laboratories of the University of Texas at Austin (ARL:UT) in the 1990s. Dr. Muir continued the seismic SONAR research at the Naval Postgraduate School when he became the Chair Professor of Mine Warfare. The previous contributions of the research done by ARL:UT and Naval Postgraduate School will be briefly discussed in the following sections.

## A. ARL:UT

Based on the concept that Rayleigh waves can be used to detect buried mines, an experimental device was developed by ARL:UT. The seismic wave source consisted of an electro-mechanical transducer that can drive a six-inch by eight-inch exciter foot with 43 protruding nails on the bottom. The transducer can generate seismic vibrations into the ground and stabilizes the source. The receiving array consisted of three three-axis geophones. [Ref. 8] Figure 10 shows the device.

The experiments done by ARL:UT showed that, because of the reverberation and the reflections of the body wave that the receivers registered, the target signal was masked. By using some signal processing techniques to isolate the target signal, the target was detected successfully.

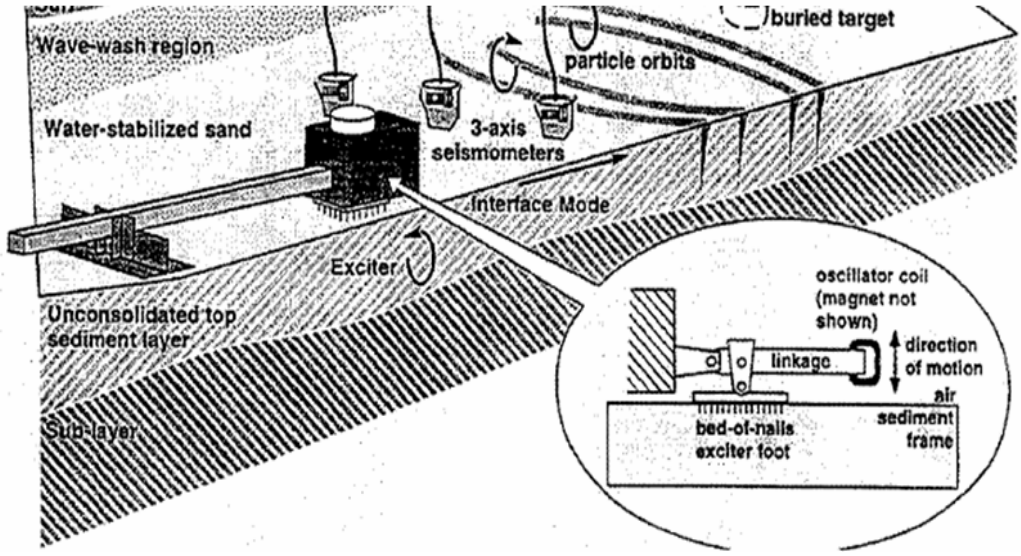


Figure 10. ARL:UT Seismic SONAR Device [Ref. 8]

## B. NPS

In 1998, Lt. Frederick E. Gaghan (USN) designed a discrete-mode seismic SONAR source to generate Rayleigh waves. [Ref. 8] Also in 1998, Lt. Sean M. Fitzpatrick (USN) and Maj. Patrick W. Hall (USA) worked together on the seismic SONAR. Lt. Fitzpatrick (USN) developed two vertical-motion electro-mechanical linear actuator sources to generate Rayleigh waves. [Ref. 11] Maj. Hall's thesis research focused on target strength. He found that target strength increased with increasing mass of the target. [Ref. 12] In 2000, Lt. Kraig E. Sheetz (USN) showed that a buried seven-element vertical shaker line array formed a narrow beam of Rayleigh wave energy and the experimental results also showed that the seismic SONAR is useful for buried mine detection. [Ref. 5] The buried seven-element line array was well-coupled to the earth, however, it lacked mobility. Previous works in mobile source development were also conducted. In 2002, Lt. Scott C. McClelland (USN) developed a rolling line source used as a seismic-acoustic SONAR source. [Ref. 13] Figure 11 shows the rolling line source element and the shaker assembly mounted inside.

Figure 11. Rolling Line Source

In 2003, Ens. Douglas MacLean (USN) developed a small tracked vehicle with dual inertial mass shakers mounted on top and used it as a mobile seismic source. [Ref. 15] Figure 12 shows the mobile source vehicle.

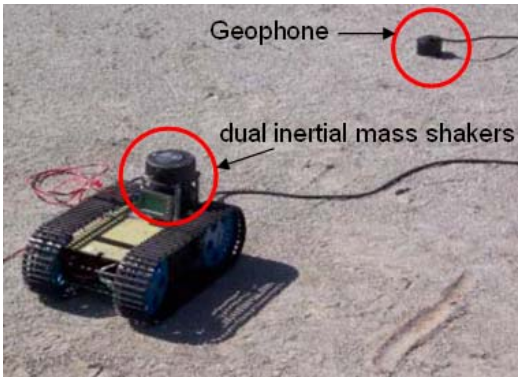


Figure 12. Mobile Seismic Source

In his design, the source was mobilized, but had poor ground coupling. In 2003, Lt. Steven E. Rumph (USN) developed a four-element end-fire array as a seismo-acoustic SONAR source. His results demonstrated fair unidirectionality; measured front-to-back rejection was 10-12dB. [Ref. 10]

THIS PAGE INTENTIONALLY LEFT BLANK

# IV. EQUIPMENT

## A. LISTING

**1. Source:** 24 AURA Bass Shakers, model AST-1B-4. Peak force: 20lb (90N)

**2. Receiver:** SENSOR Nederland (a subsidiary of Input/Output, Inc.), SM-11 geophone. Seismometers are composed of SM-11 geophones.

**3. Accelerometer:** PCB Piezotronics, Inc. Model 354B33, sensitivity 10.2mV/g.

**4. Function Generator:** Three Hewlett Packard 3314A's

**5. Driver:** Three Carvin 1000 Watt Power Amplifiers, Model DCM 1000

**6. Accelerometer Amplifier:** PCB Piezotronics, Inc. Model 482A17

**7. Oscilloscope:** Tektronix TDS 3014 and TDS 3034, Four Channel Color Digital Phosphor

**8. Power Generator:** Honda EU2000i, 3.5 HP, Single Cylinder, AC output 60 Hz, 120V, 13.3A

**9. Transportation:** Polaris Ranger 6X6 EFI, 70 HP.

**10. 8-channel Dynamic Signal Analyzer:** Scientific Atlanta (now Cognitive Vision) model 390.

## B. DESCRIPTION

### 1. Seismo-Acoustic Line Source

The source is composed of 24 AURA “Bass Shakers”. The bass shaker is a moving magnet transducer (an inertial mass shaker), which is an electromechanical device that can convert electrical energy into motion. It is used by the automobile audio industry as a low frequency vibration source. The source-to-ground coupling mechanism of the transducer provides the means by which the output mechanical energy can be transmitted into the medium.

The idea of the source design came from Prof. Baker and the source was made at NPS. The source is a 2-degree-of-freedom (2-DOF) transverse line source which is composed of six modules, divided into three sets of two modules each, with 2 horizontal and vertical shakers in each module, for a total of 24 shakers. These are mounted on a common base plate. Each shaker is capable of producing 20 lb (90N) of peak force. The idea of a 2-DOF source was to selectively generate a Rayleigh wave. The vertical shakers in each set are connected together, as are the horizontal shakers. The radial and vertical shakers in each subset are driven by one amplifier channel, so as to produce elliptical motion by adjusting the amplitude and phase of the driven signal to each. All the vertical shakers were driven the same, as were all the horizontal shakers. Figure 13 shows the design concept of the source. The upper right figure depicts a multitude of “spikes” on the bottom of the base plate, to facilitate radial motion coupling. In the source as constructed, a pair of narrow strips of metal approximately 2.5cm in height were employed instead. The weight of the source provides good vertical motion coupling. Concepts to mobilize the source are shown in the lower left and right. The source used in this research was not mobile.

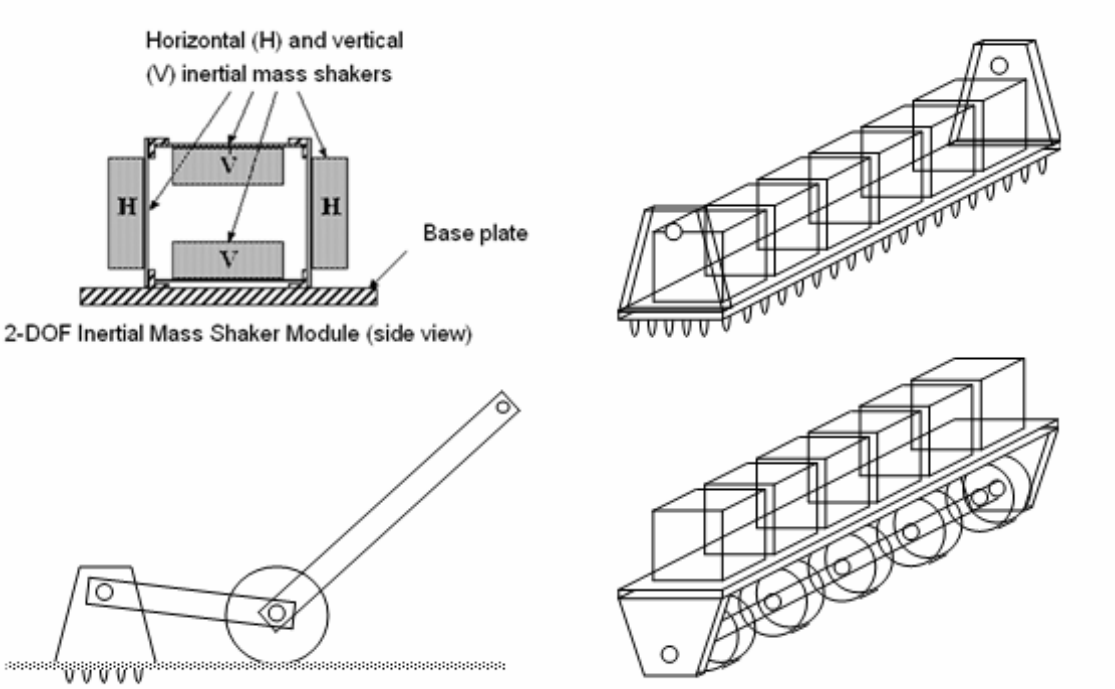


Figure 13. Mobile 2-DOF Rayleigh Wave Source Array Concept

The length of the source is 46 inches (1.17m), the width is 6 inches (0.15m) and the weight is 126 pounds (562N). The weight of the source provides good vertical coupling. Figures 14 and 15 show the source configuration. Shown are the six modules, with vertical and horizontal mounted shakers. A triaxial accelerometer was mounted on the center of the base plate. For excitation, there are six amplifier channels driving the three sets of two modules, vertical and horizontal separately. Appendix A shows the specification of the AURA Bass Shakers, model AST-1B-4.

Figure 14. Seismo-Acoustic SONAR Source Configuration

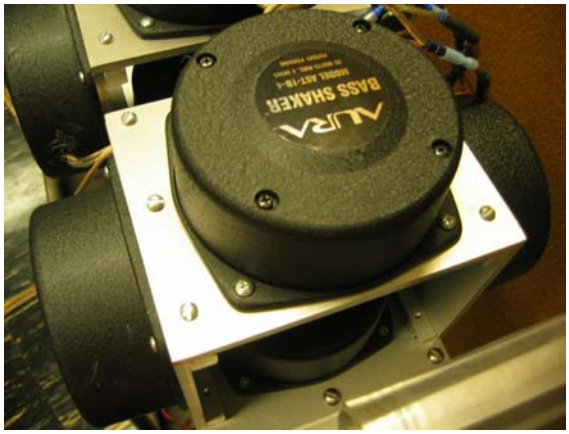


Figure 15. One Module of the Source

In each set of shakers, the orientation of the two vertical ones is the same, and the other two on the sides are mounted in opposite orientation. This means one of the side mounted shakers needs to be energized out of phase with the other in order to produce motion in the same direction. Therefore, the side shakers are connected positive to negative and the vertically mounted shakers are connected positive to positive. Each module has two sets of shakers connected in parallel, while the vertically and horizontally mounted shakers in each set of two modules were connected in series. Figure 16 shows the wire

connection of the 8 shakers in each set and the black arrows show the orientation of the shakers. (arrow points toward top of case)

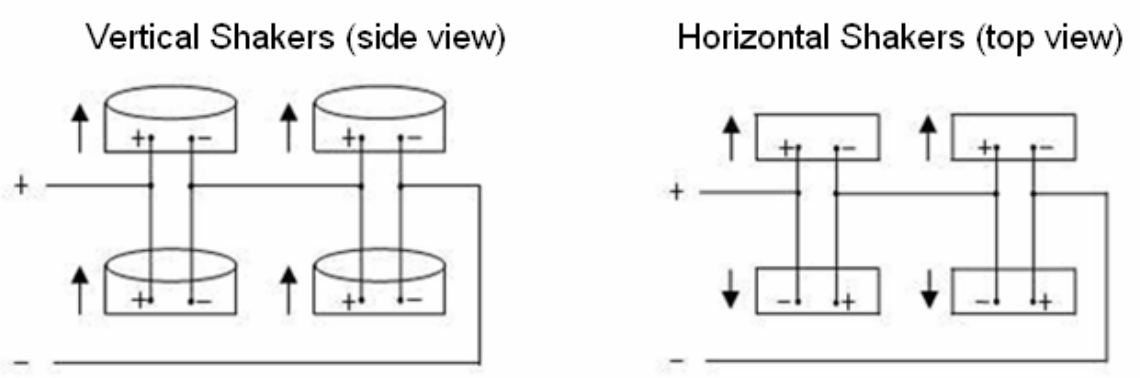


Figure 16. The Wiring of the Vertically- and Horizontally-Mounted Shakers

The six shakers modules, mounted on the base plate, constitute an extended coherent source, and should produce directionality perpendicular to its long dimension. The source also has the ability to create elliptical particle motion, with independent vertical and horizontal shakers.

The concept of the source design in this research is similar to that of Frederick E. Gaghan's source design in 1998, in that it has two degrees of freedom. It differs from Gaghan's source, however, in that it employs vertical and horizontal shakers, whereas Gaghan's source employed two shakers at ±45 degrees with respect to the earth. [Ref. 8] The reason to for a two degree-of-freedom source is to try to selectively generate unidirectional Rayleigh waves. Therefore, one goal of present research was to investigate if this source, which can produce elliptical motion, can achieve forward directionality. This, as an alternative to an end-fire array source, which was Steven E. Rumph's source design in 2003.

## 2. Ground Motion Sensors

Two types of ground motion sensors were employed in the present research. Three-axis geophones were deployed to measure the radial and vertical components of surface velocity of the radiated Rayleigh wave. A three-axis accelerometer, attached to the source base plate, was employed to measure the source motion.

The three-axis geophones used in this thesis research were designed and built by NPS engineer Mr. Jay Adeff. They are composed of three SENSOR Nederland uniaxial SM-11 Geophones, mounted in X, Y and Z coordinate directions (two mounted in a horizontal direction, X and Y, one in the vertical direction, Z) and potted in a watertight cylinder. Once the geophones were potted in the cylinder, Lt. Steven E. Rumph used a pendulum calibration device consisting of a threaded rod with a weight attached to the bottom to determine the positive X-Y-Z axis directions. [Ref. 10] Appendix B shows the specification of the SM-11 Geophone. Figure 17 shows the three-axis geophone and the three uniaxial geophone components before being potted.


Figure 17. Three Component Geophone

The triaxial accelerometer was mounted on the center of the base plate of the line source. See Figure 18. Appendix C shows the specification of the accelerometer, PCB Piezotronics, Inc. Model 482A17.

Figure 18. The Accelerometer Mounted on the Plate

When both the geophone and the accelerometer are placed on the source, the acceleration can be measured with the mounted accelerometer and the velocity with the geophone. By either comparing the time-integrated accelerometer signal to the geophone signal, or comparing the time-differentiated geophone signal to the accelerometer signal, similar results will be obtained. The dynamic signal analyzer can do either integration or differentiation. It is preferable to integrate, since it suppresses the noise more effectively. The only problem with doing this is that any DC signal present in the accelerometer output is an error and will integrate to a linear trend with time, which would have to be removed before comparing against the geophone signal. Differentiating the geophone signal does not have this DC offset problem since the derivative of a constant is zero.

### 3. The Equipment Set Up in the Trailer

The geophone receiver panel was designed to handle up to eighteen 3-axis geophones at once. It was designed by Lt. Rumph and constructed by NPS

electronics technician, Mr. Sam Barone. See Figure 20. There are three large 36-pin connectors at the bottom of the panel. Each connector allows six 3-axis geophones to be connected at once. These connectors were used for the geophone signal input. In this research, only one 36-pin connector was used to connect the six 3-axis geophones. For each 36-pin connector, there are 18 BNC connectors mounted right above the 36-pin connector. These 18 connectors are divided into three groups labeled X, Y, and Z, which represent the X, Y, and Z component signal outputs of the 3-axis geophones.

Once the geophones and the panel were connected, the radial (X) and vertical (Z) velocity output signals were sent to the signal analyzer, DynamicPro Signal Analyzer Model 390, using the BNC connectors. The analyzer was also mounted in the trailer and was used for data collection. Appendix D provides the specifications of the analyzer. The data analysis and signal processing methods are summarized into 4 steps, shown Table 1.

| STEP | COMPUTER | OPERATION |
|---|---|---|
| 1 | Analyzer | Record the accelerometer and seismic geophone signals. |
| 2 | Analyzer | Export trace data. (txt file) |
| 3 | Analyzer to laptop | Download the txt files. |
| 4 | Laptop | Signal analysis using MATLAB program. |

Table 1. Summary of Data Acquisition and Signal Processing Steps

There are eight signal input channels on the analyzer. Six channels were used to record three radial and three vertical signal inputs coming from the output of the geophone panel and two channels were used to record the radial and vertical accelerometer signals coming from the accelerometer amplifier. The gain

of the accelerometer amplifier was set to be 1 before testing on the beach. Figure 19 shows the author at the controls of the analyzer.

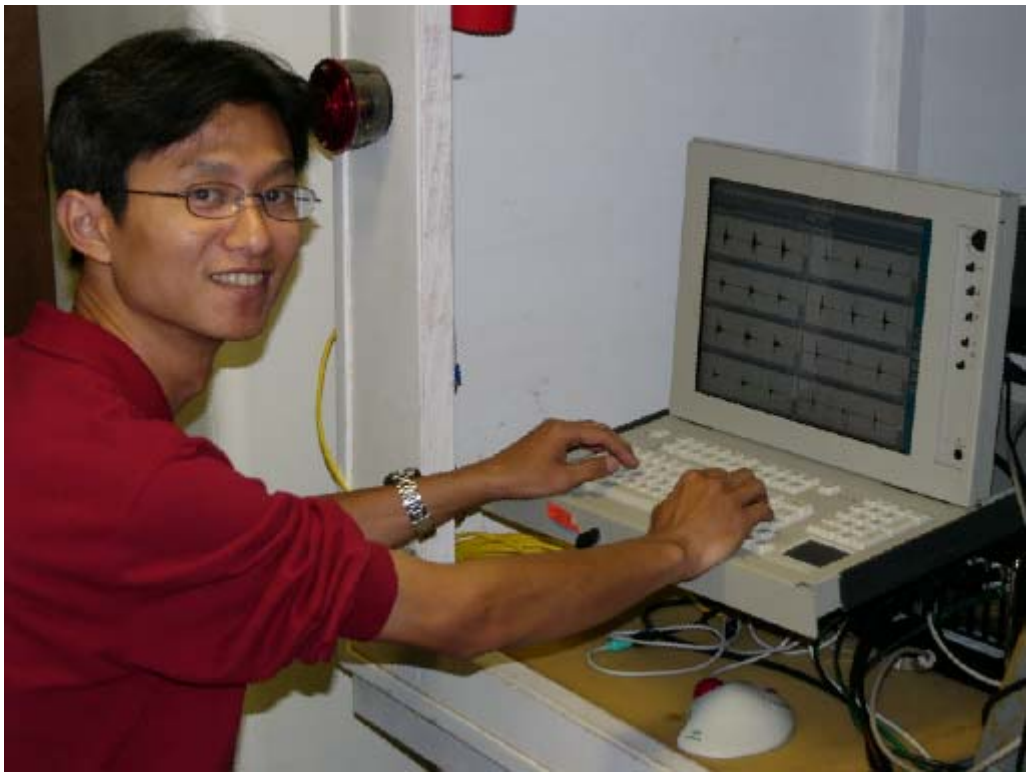

Figure 19. DynamicPro Signal Analyzer Model 390

The HP 3314A Function Generators were used to generate various transient waveforms to drive the line source. There are three function generators. One was used to amplitude modulate the other two. The carrier phase and the amplitude of the other two can be varied to produce linear or elliptical source motion. The signals can be monitored on the oscilloscopes. The Carvin Power Amplifiers were used to amplify the signal from the function generators and output the signal to drive the line source. The power supply used on the beach was the HONDA EU 2000i generator. When operating on the beach, noise and vibration from the generator can cause interference with the seismometer output signal. In order to prevent this interference, the generator was put far away from

the line source (on the bluff) or set on the trailer tow vehicle instead of on the sand beach. Figure 20 shows the equipment mounted in the trailer.

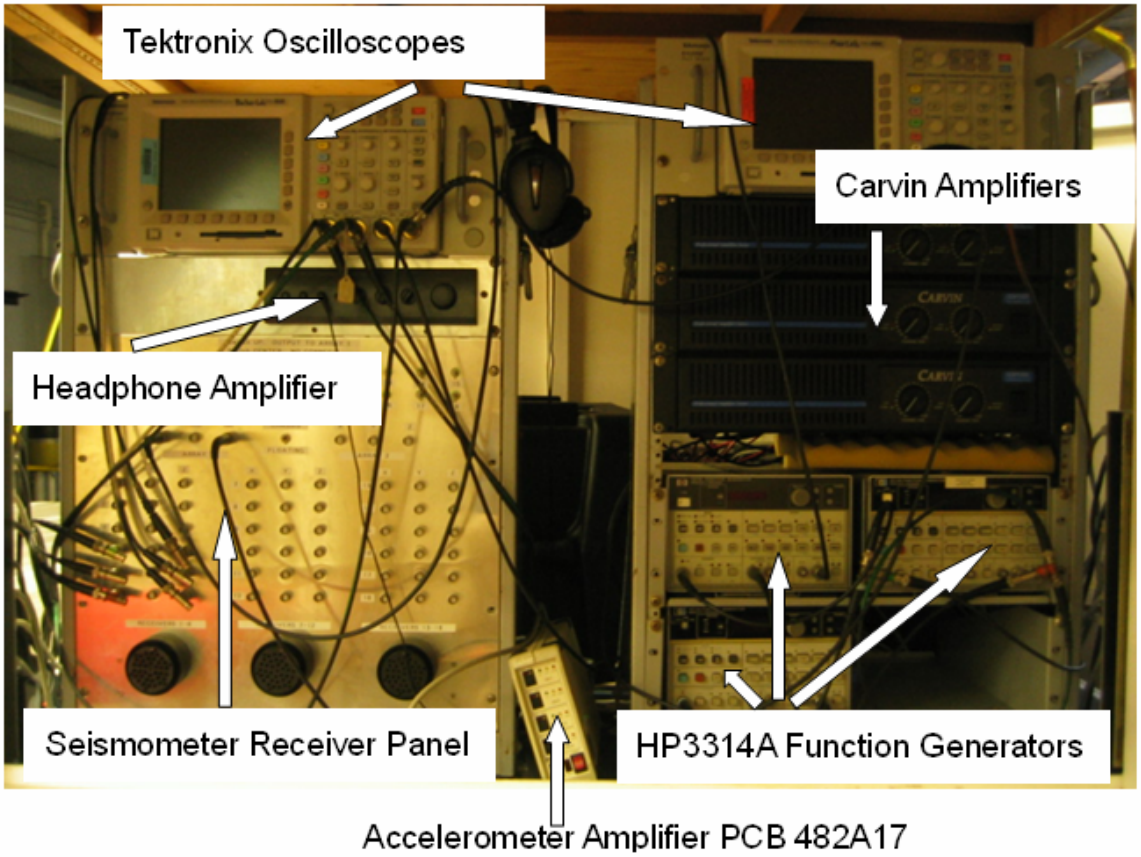


Figure 20. Field Testing Equipment Mounted in the Trailer

One problem that needed to be addressed was that the 36-pin geophone connectors often made poor contact, causing capacitive-coupled electrical crosstalk between the drive signal and the geophone output. By ensuring that the connector was clean and lubricated, without sand on it, and plugged in completely to make a good connection, the electrical crosstalk problem was fixed. [Ref. 10]

# V. FIELD TESTS AND RESULTS

## A. SOURCE EXCITATION

The waveform that was used to drive the amplifiers was a 5-cycle tone burst, amplitude-modulated by a single-cycle haversine waveform. The haversine function is defined by,

$$haversin(\theta) = sin^2(\frac{\theta}{2}).$$

Based on past and present experience, a Rayleigh wave speed of about 90m/s was expected, and so a carrier frequency of 100Hz was selected, corresponding to a wavelength and penetration depth of approximately one meter. Figure 21 shows the waveform of the single-cycle haversine (produced by MATLAB). This was chosen as an amplitude modulation waveform because it has a smooth turn-on and turn-off, and it can be produced by the function generator employed.

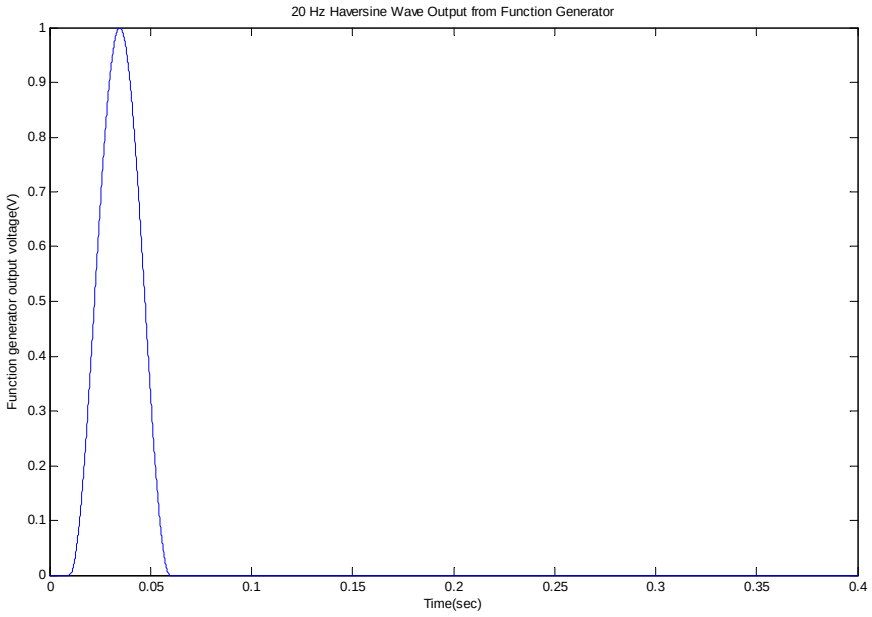


Figure 21. Function Generator Output: 20 Hz Haversine Wave Signal

The function generator settings are listed in Table 2. The amplitude values listed in Table 2 for the radial and vertical excitation were the initial voltage values on the function generators. These values were varied and the actual peak excitation voltage values from the power amplifier were recorded.

| | Freq(Hz) | Ampl.(V) | Offset(V) | Sym(%) | Phase | N cycle |
|---|---|---|---|---|---|---|
| Function Generator (ampl. modulation) | 20 | 1.06 | 0 | 50 | -90 | 1 |
| Function Generator (excite radial) | 100 | 1.25 | 0 | 50 | -90 | 5 |
| Function Generator (excite vertical) | 100 | 1.25 | 0 | 50 | 0 | 5 |

Table 2. Function Generators Settings

The single-cycle haversine wave was produced by shifting the phase of a single-cycle sine wave by 90 degrees and adjusting the offset to be zero. The driving frequency of the one cycle burst haversine signal was 20 Hz (0.05 seconds). The sample rate of the signal analyzer was set to be 10240 samples per second. For each run, data records were collected for 400 milliseconds (4096 samples). The analyzer has a full-scale resolution of 16 bits (1 part in 32768).

As described in Chapter II, in a Rayleigh wave, the radial motion leads the vertical motion by 90 degrees. This phase relationship causes the particle motion to be elliptical. To produce such elliptical particle motion, the phase of the function generator that drives the radial shakers was set at 0 degrees, giving a cosine wave, and the phase of the function generator that drives the vertical shakers was set at ±90 degrees, giving a sine wave. Figures 22 and 23 show example wave packets of the input signal (using MATLAB), used to excite the desired radial and vertical motion.

The resulting radial and vertical driving signals produced an elliptical motion at the source, which is optimum for generating a Rayleigh wave. The ratio

of the amplitude of the vertical component to that of the radial component was adjusted to produce a ratio of vertical motion to radial motion of the source of approximately 1.5 by varying the signal generator amplitude and observing the response of the output signals of the accelerometer mounted on the source.

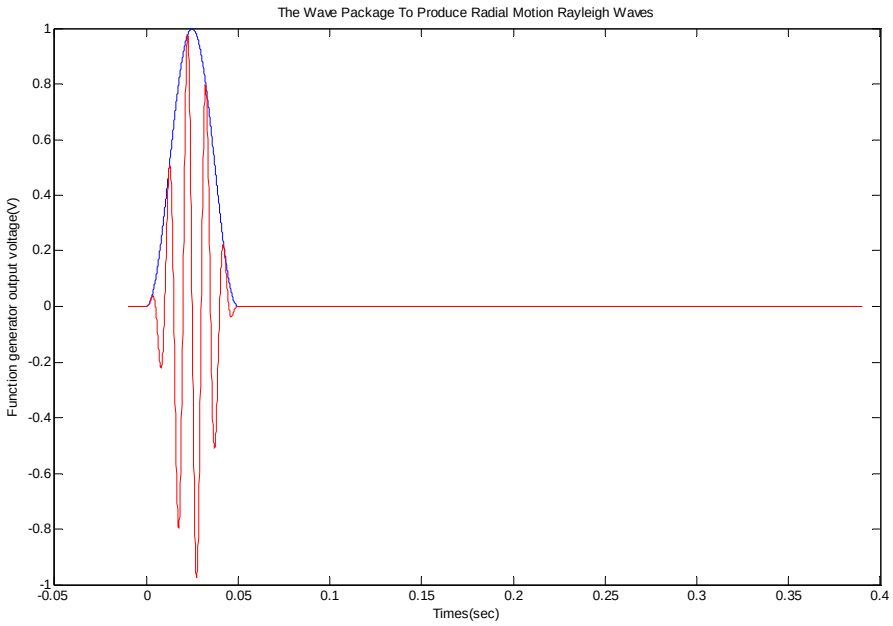


Figure 22. Example Radial Shaker Drive Signal

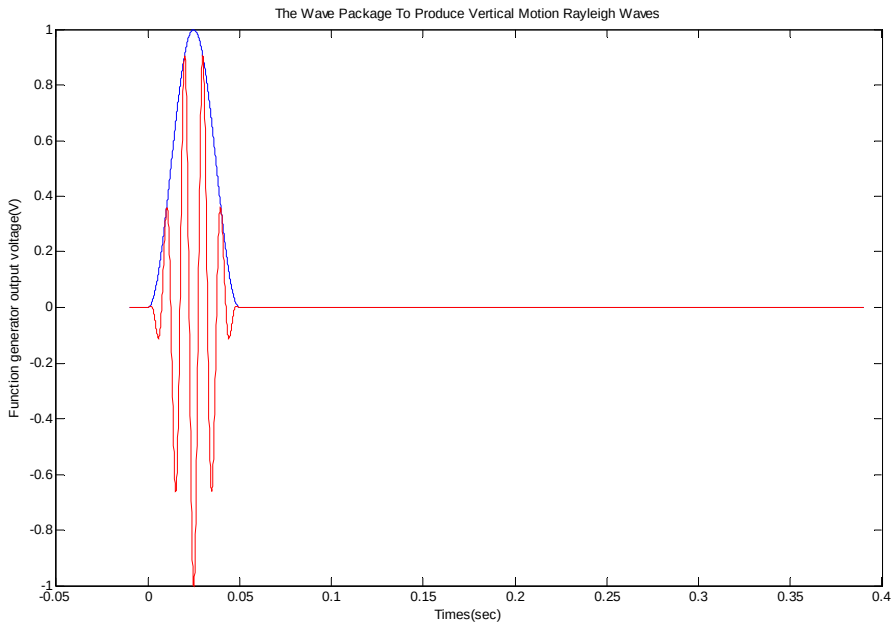


Figure 23. Example Vertical Shaker Drive Signal

## B. BEACH TESTING

Field tests of the source were conducted five times between August 12 and October 23, 2005. Six three-axis geophones were set up in various linear and angular configurations to measure the Rayleigh wave speed and the source beam pattern.

The geophones were placed at certain positions (distances and angular positions), making sure that the positive X direction marked on the geophones was oriented radially away from the source, because a cylindrical coordinate system was employed. The testing site was at the NPS beach research site on Del Monte Beach, Monterey. Figure 24 shows the beach testing site.


Figure 24. Field Testing Site at Del Monte Beach

## C. RAYLEIGH WAVE CONFIRMATION

As mentioned in Section II. B, the radial component of Rayleigh wave surface motion leads the vertical component by 90 degrees, which produces a retrograde elliptical particle motion. To confirm that the source generates a Rayleigh wave, the radial and vertical geophone signals are plotted versus time in three dimensions using MATLAB, referred to as a Hankel plot.

Figures 25, 26 and 27 show example Hankel plots illustrating Rayleigh wave propagation. In each figure, the 3-D plot in the upper left shows the accelerometer signal. The other three plots show the signals received by three geophones placed in a line at distances of 3 ft (0.91m), 15 ft (4.57m) and 27 ft (8.23m). Also see the geophones layout in Figure 28. In Figure 25, vertical source excitation only was used. Figure 26 shows the Hankel plot of Rayleigh wave propagation with both radial and vertical source excitation, and vertical phase -90 degrees relative to radial (retrograde), Figure 27 with vertical phase +90 degrees (prograde). The peak value of the amplifier radial output voltage

was 25V and vertical 50V. The wave packet carrier frequency was set to be 100 Hz. The green curves in each plot represent the path of the wave propagation projected onto a plane. This provides an easy way to confirm that the particle motion is elliptical. Elliptical motion is definitely observed in all cases for ranges of 15 and 27 feet, confirming the presence of a Rayleigh wave. Depending on the elapsed time, the range, and the excitation, both retrograde and prograde motion are observed, with varying relative amplitude of vertical to radial motion. Also, there does not appear to be any systematic dependence of the nature of the radiated waves on the relative amplitude and phase of the radial and vertical excitation. This was not an expected result.

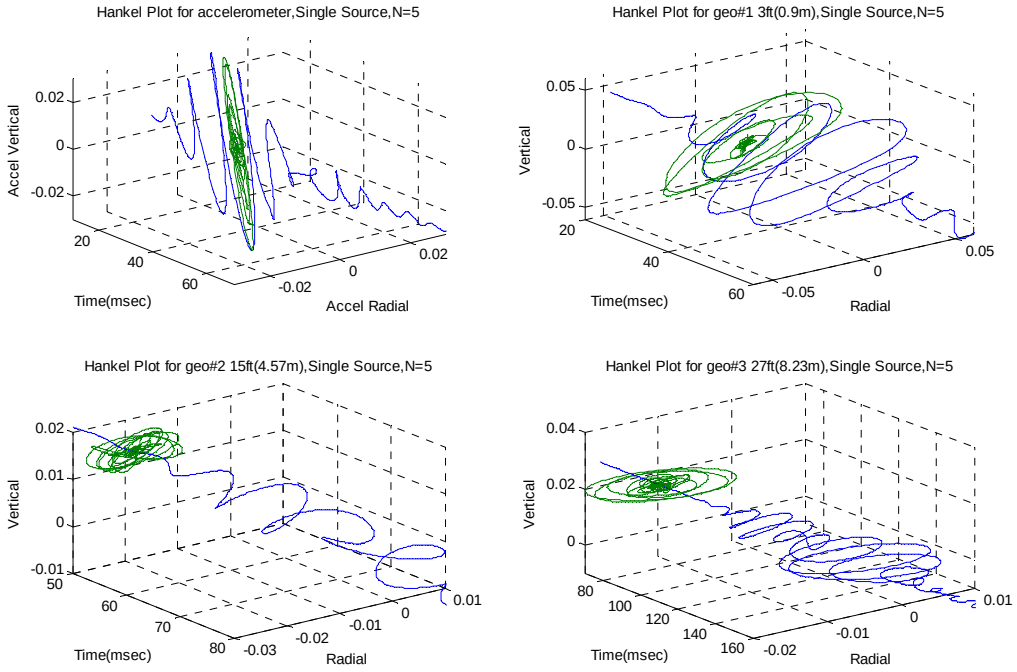


Figure 25. Hankel Plots, Vertical Excitation Only

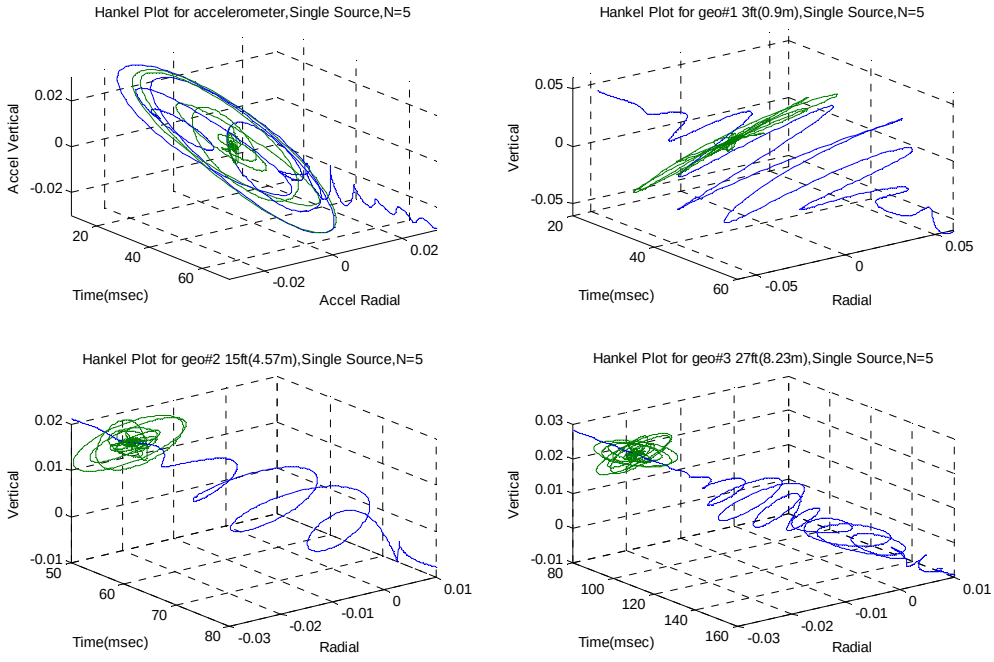


Figure 26. Hankel Plots, Radial and Vertical Excitation; Vertical Relative Phase -90 Degrees

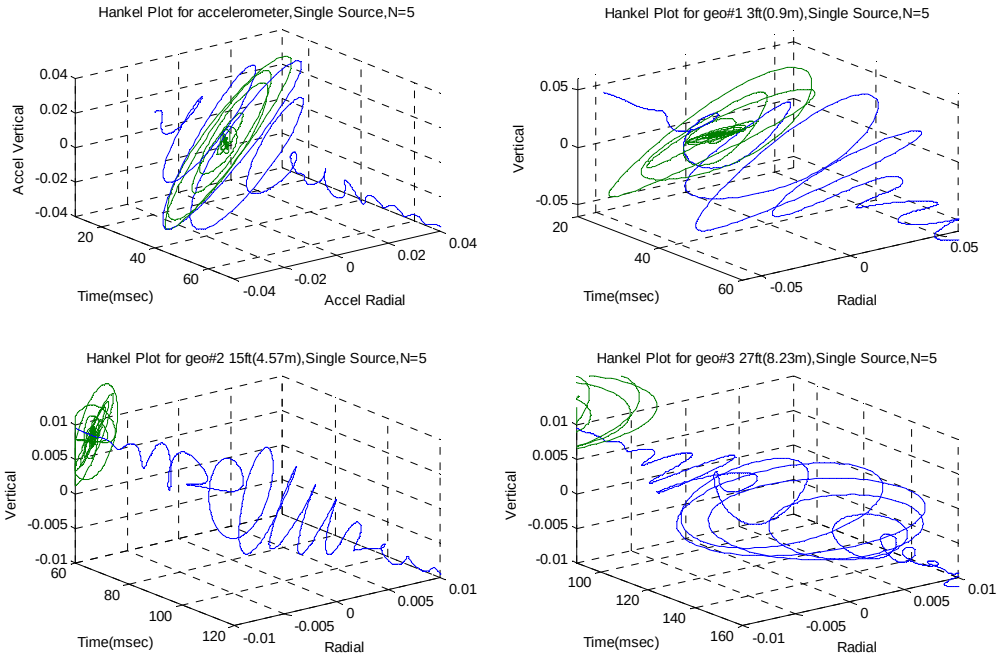


Figure 27. Hankel Plots, Radial and Vertical Excitation; Vertical Relative Phase +90 Degrees

## D. VECTOR POLARIZATION FILTERING

As mentioned in the prior discussion of the nature of Rayleigh waves, the radial and vertical components are 90 degrees out of phase. This phase relationship causes the elliptical particle motion. Vector polarization filtering is a method that can help filter out unwanted waves, waves that have radial and vertical components in phase, in favor of Rayleigh waves.

If the phasor radial and vertical ground velocities are $\vec{R}$ and $\vec{V}$, the vector polarization filtered signal, which we term the Complex Power, is taken to be $\vec{R}\,\vec{V}^{*}$, where $\vec{V}^{*}$ is the complex conjugate of $\vec{V}$. The phasors $\vec{R}$ and $\vec{V}$ are obtained from the measured real-valued radial and vertical velocity signals by a Hilbert transformation operation in MATLAB.

radial velocity signal, $\vec{R} = R\,e^{j(\omega t+\phi_r)}$,

vertical velocity signal, $\vec{V} = Ve^{-j(\omega t+\phi_v)}$,

complex power signal, $\vec{V}^{*}\vec{R} = VR\,e^{j(\phi_r-\phi_v)}$

Complex power is not really a power, but since it is the product of the two velocities with complex conjugate, it is referred to as complex power. The use of complex power in data processing helps to suppress other than Rayleigh waves, as explained below.

For retrograde elliptical motion, the radial velocity phasor leads the vertical velocity phasor by 90 degrees. The complex conjugate of the vertical velocity phasor is taken and then multiplied, data point by data point, by the complex radial velocity phasor. The $e^{-j\omega t}$ term is canceled, and the product of the magnitudes of the radial and vertical components times a phasor depending only upon the difference between the radial and vertical phase is left.

The imaginary part of this complex power signal is simply the product of the magnitudes of the radial and vertical components multiplied by the sine of this phase difference,

$$\mathrm{Im}[\bar{V} * \bar{R}] = VR\sin(\phi_r - \phi_v).$$

The unwanted signals, for which the phase difference is zero, will be equal to zero. Therefore, they are filtered out. A Rayleigh wave will result in an imaginary part of the complex power signal that is the product of the magnitudes of its radial and vertical components. If the medium were a homogeneous, isotropic half-space, this filtering operation would perfectly capture only the Rayleigh wave. In reality, reflections from layers and other nonideal effects contaminate the results. Nevertheless, vector polarization filtering has proved useful to at least partially suppress other than Rayleigh waves.

## E. IN-SITU RAYLEIGH WAVE SPEED DETERMINATION

With transient excitation, Rayleigh wave speed can be calculated by cross correlating the received geophone signals with each other or with the source accelerometer signals (see the MATLAB program code in Appendix E). Cross-correlation of the signals was used to determine the time it took for the wave to propagate from one receiver to another, or from the source to a receiver. Since it performs an integration over all time, cross correlation analysis utilizes all of the data. Based on the distance between source and receiver and the time delay for the maximum positive correlations, the Rayleigh wave speed can be calculated quickly.

### 1. Geophones Placed in Line Positions

A linear geophone layout was employed during beach field testing on Aug 12, 2005. Geophones G3, G2 and G1 were placed at the ranges 6 feet 9 inches (2.74m), 18 feet 8.5 inches (5.71m) and 30 feet 5 inches (9.27m). The three geophones were in a line on one side of the source and perpendicular to the axis of the source. Figure 28 shows the geophone layout on the beach.

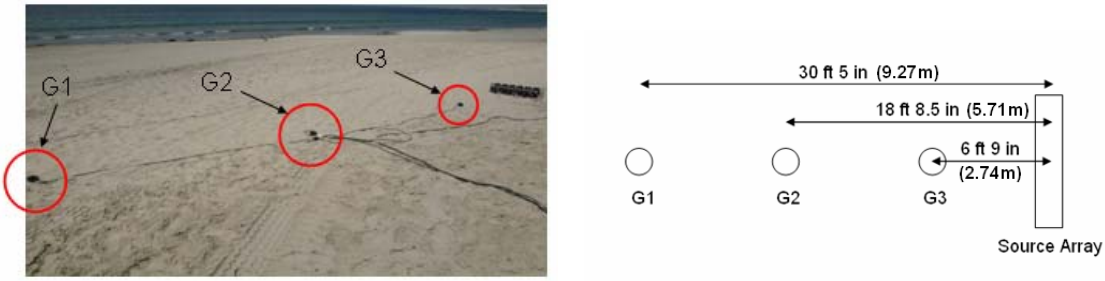


Figure 28. Geophones Placed In Line (12 Aug 2005)

The shakers were excited with the 5-cycle wave packet described in Section V. A. The carrier frequency was 100 Hz, analyzer sample frequency 10240 Hz, and sample time 1/10240 second. No signal averaging was employed. First, we drove the vertical shakers only. Second, we drove the radial shakers only. Lastly, we drove both radial and vertical shakers with radial phase 0 and vertical phases of ±90, ±60 and ±30 degrees. Collected data were 5-point smoothed using the MATLAB smooth function with N=5. The peak value of the amplifier radial output voltage was 25V and vertical 50V. Table 3 provides the average observed wave speeds for different source settings, as determined by cross-correlation. As shown in Table 3, the radial and vertical wave speeds are approximately equal to 96m/s.

| Array setting | Phase(degrees) Vert./Rad. | Avg. radial wave speed | Avg. vertical wave speed | Complex PWR avg. speed |
|---|---|---|---|---|
| Vertical only | -90 | | 96.35m/s | 95.50m/s |
| Radial only | 0 | 92.45m/s | | 69.97m/s |
| Both vert & rad on | -90/0 | 96.18m/s | 95.81m/s | 103.24m/s |
| Both vert & rad on | +90/0 | 96.02m/s | 95.98m/s | 103.11m/x |
| Both vert & rad on | +60/0 | 96.05m/s | 96.14m/s | 103.27m/s |
| Both vert & rad on | +30/0 | 96.04m/s | 96.23m/s | 101.66m/s |
| Both vert & rad on | -30/0 | 90.40m/s | 132.45m/s | 105.12m/s |
| Both vert & rad on | -60/0 | 96.35m/s | 95.83m/s | 104.72m/s |

Table 3. Wave Speeds Determination of Geophones Placed in Line (100Hz)

### 2. Geophones Placed Both in Line and Angular Positions

Two different geophone layouts were employed in this field testing. In one layout, geophones G1, G2, and G3 were placed in a line at ranges of 3 feet (0.91m), 15 feet (4.57m) and 27 feet (8.23m). G4, G5 and G6 were placed at ranges of 15 feet, with G4 and G5 at angles of ±45 degrees relative to G6. In the other geophone layout, G1, G2, and G3 were placed in a line at ranges of 48 ft (14.63m), and 72 ft (21.95m). G4, G5, and G6 were placed in a line parallel to the source, at a separation distance of 60 feet. Figures 29 and 30 show the geophone layouts on the beach.

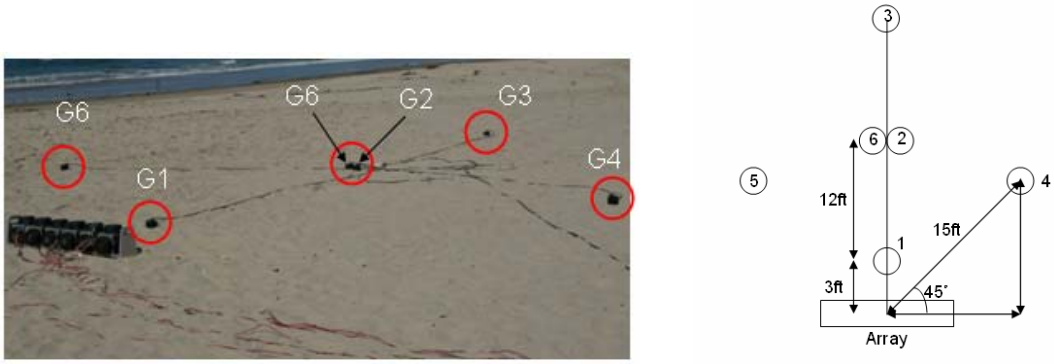


Figure 29. Geophones Placed Both in Line and in Angular Positions (5 Sep 2005)

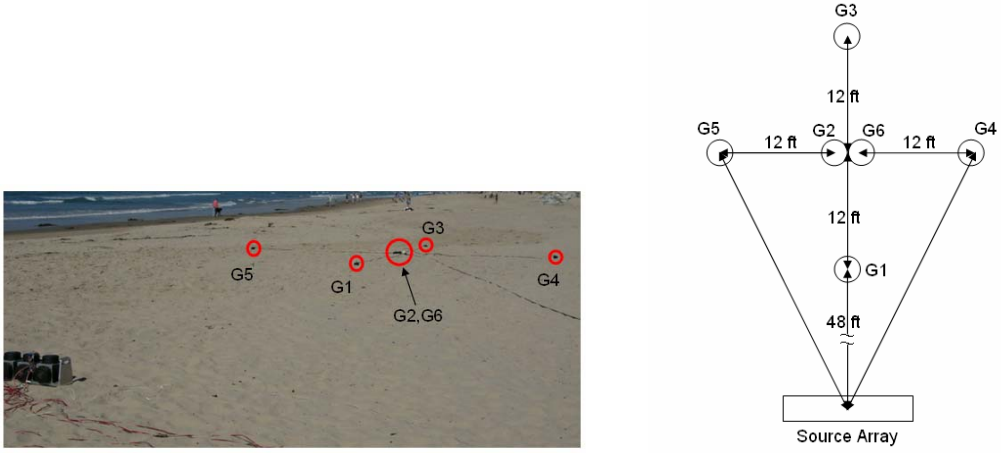


Figure 30. Geophones Layout with G1 Placed at 48 Feet from the Source (5 Sep 2005)

For both layouts, the 5-cycle wave packet with carrier frequency 100 Hz was used. The synchronous average 16 successive “shots” was records. For the two cases of geophones in line (G1, G2, G3) and in angular positions (G4, G5, G6), we drove the vertical signal only first, and then both radial and vertical signals with phase radial 0 and vertical -90 degrees. We then changed the vertical phase to +90 degrees.

Again, the average wave speed can be determined by a cross correlation calculation between geophone and geophone, and between accelerometer and geophone for G1, G2 and G3, as they are placed in a radial line. However, the average wave speed can only be determined by cross correlation between accelerometer and geophone for G4, G5 and G6, as they are not separated in range. The figures that provide the raw data are shown below. Figures 31 and 32 show the 5-point smoothed signals of G1, G2 and G3, placed in line, with vertical signal driven only, at frequency 100 Hz. The first subplot in each figure shows the accelerometer output signal (acceleration) and the other three show the received geophone signals (velocity).

In addition to the radial and vertical signal output, the imaginary power output was also calculated. Imaginary power here is used to mean the results of the process of vector polarization of the radial and vertical signals as described earlier. Figure 33 shows the plot of the imaginary part of the complex power at ranges of 3 feet (0.91m), 15 feet (4.57m) and 27 feet (8.23m).

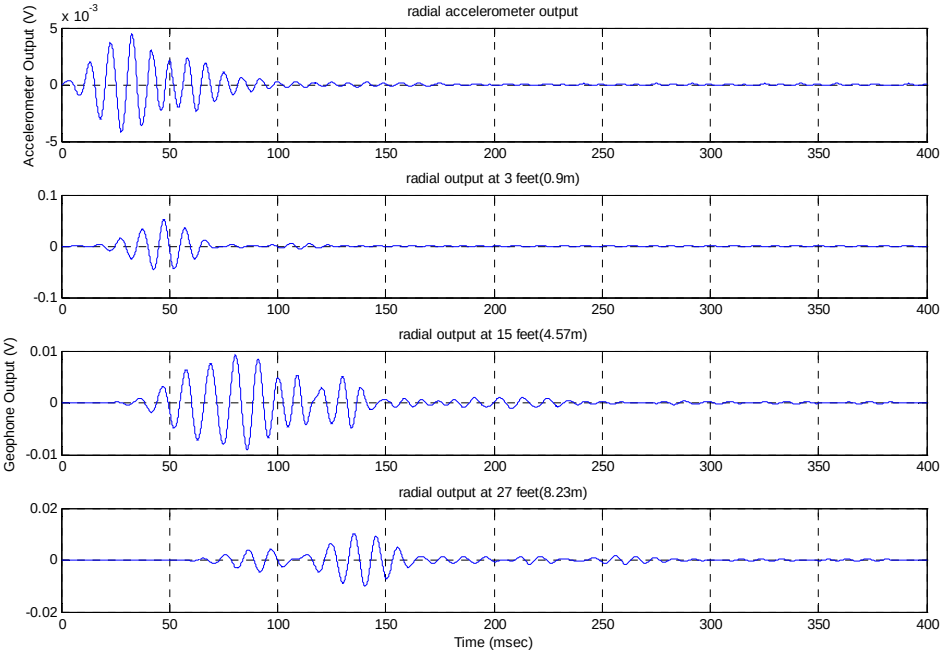


Figure 31. Received Radial Signals

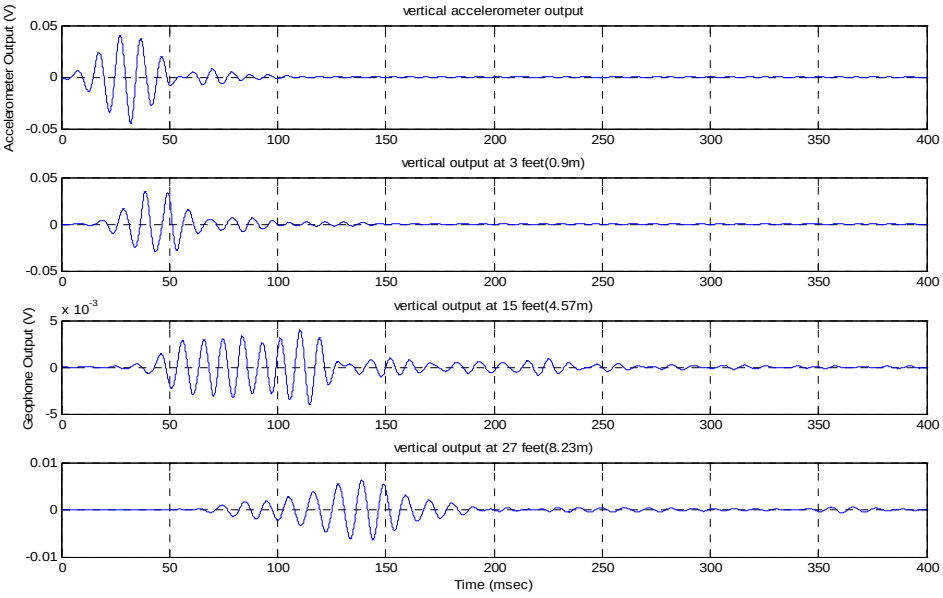


Figure 32. Received Vertical Signals

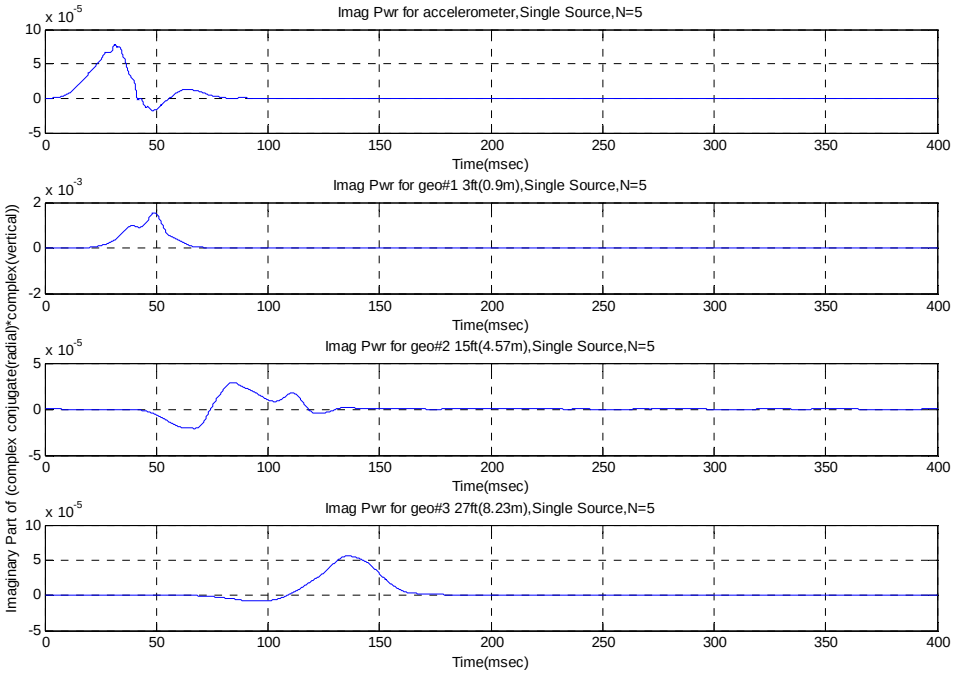


Figure 33. Received Imaginary Part of Complex Power at 3 ft (0.91m), 15 ft (4.57m) and 27 ft (8.23m)

Cross correlations were performed between geophone signals at 3 feet (0.91m) and 15 feet (4.57m), 15 feet (4.57m) and 27 feet (8.23m), and 3 feet (0.91m) and 27 feet (8.23m). The time delays for the maximum positive correlations were used to calculated wave speed. Aside from the radial and vertical wave speeds, the imaginary power wave speed was also calculated. Figures 34 and 35 show the example plots of radial and vertical correlations between geophones. Figures 36 and 37 show the example plots of the radial and vertical correlations between accelerometer and geophone. The imaginary power cross correlation plots between geophones, and between accelerometer and geophone are shown as Figures 38 and 39.

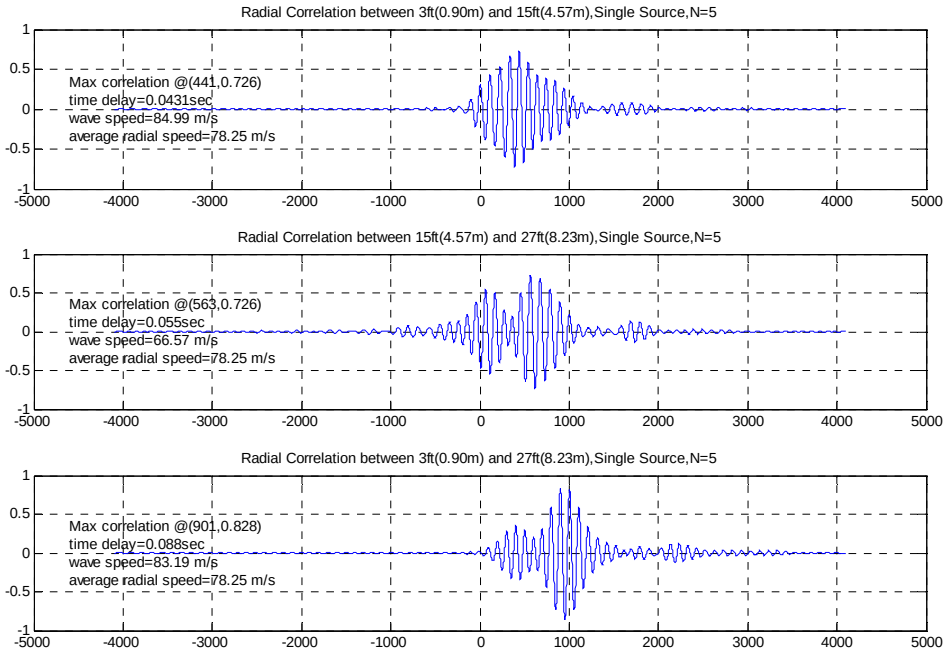


Figure 34. Radial Wave Speed Calculation Between Geophones

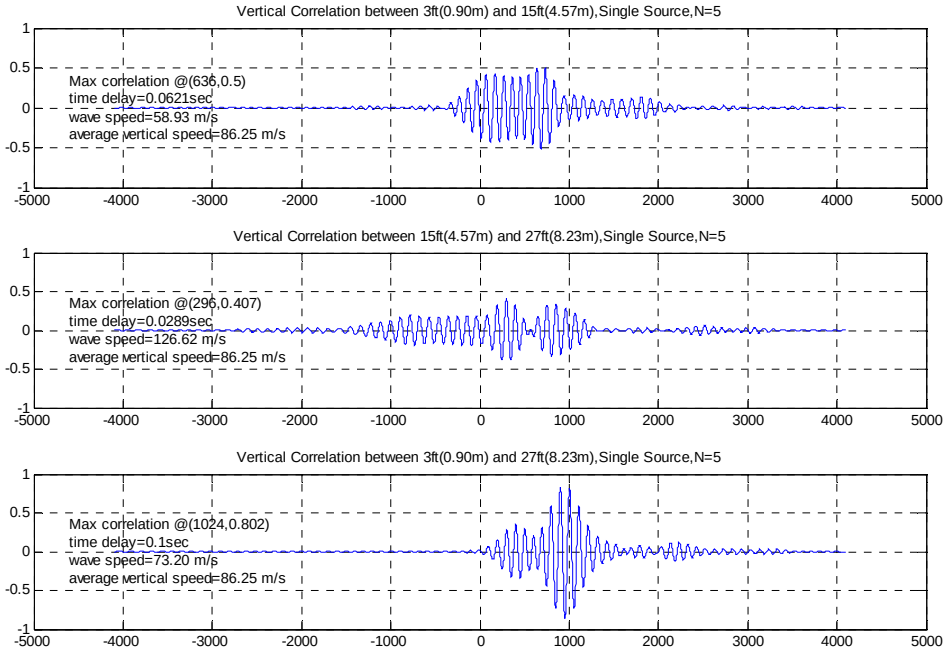


Figure 35. Vertical Wave Speed Calculation Between Geophones

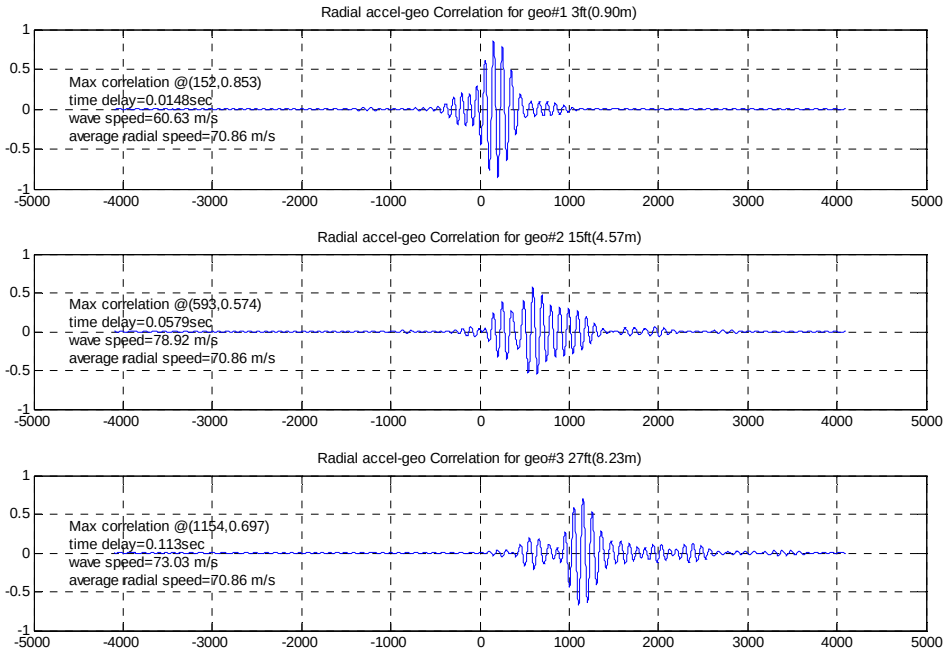


Figure 36. Radial Wave Speed Calculation Between Accelerometer and Geophone

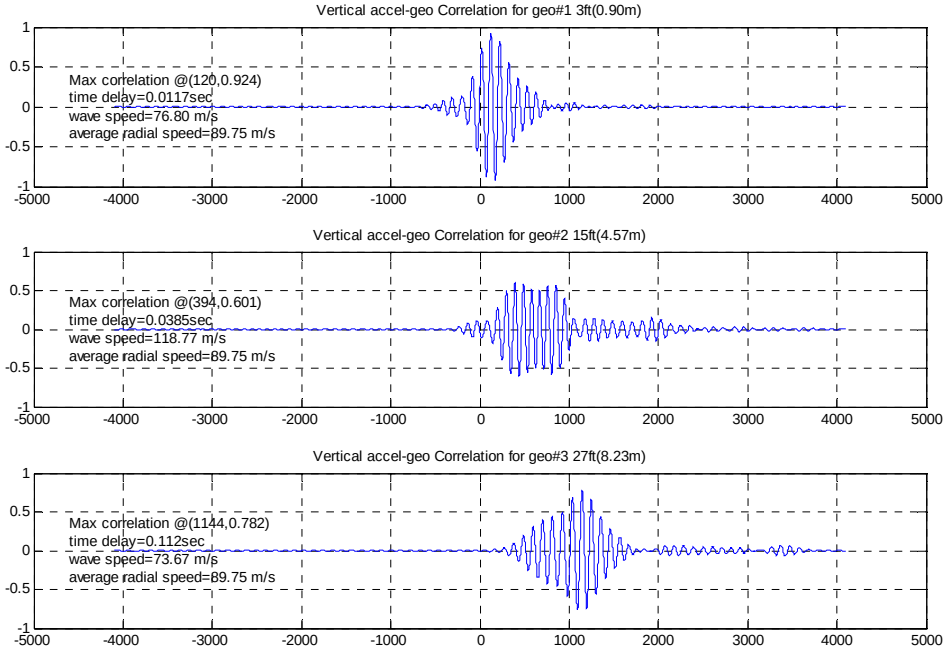


Figure 37. Vertical Wave Speed Calculation Between Accelerometer and Geophone

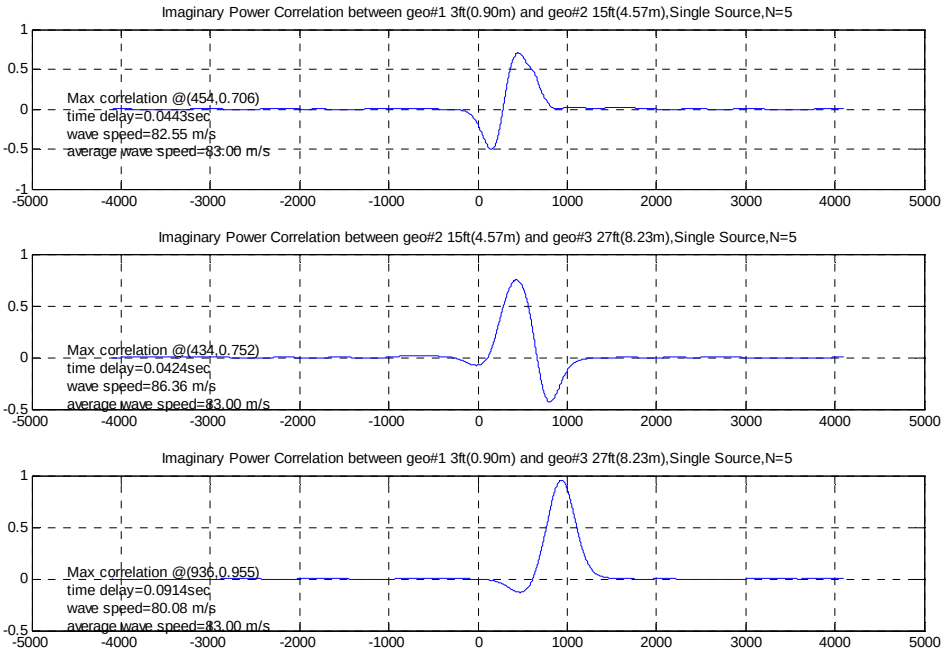


Figure 38. Imaginary Power Wave Speed Calculation Between Geophones

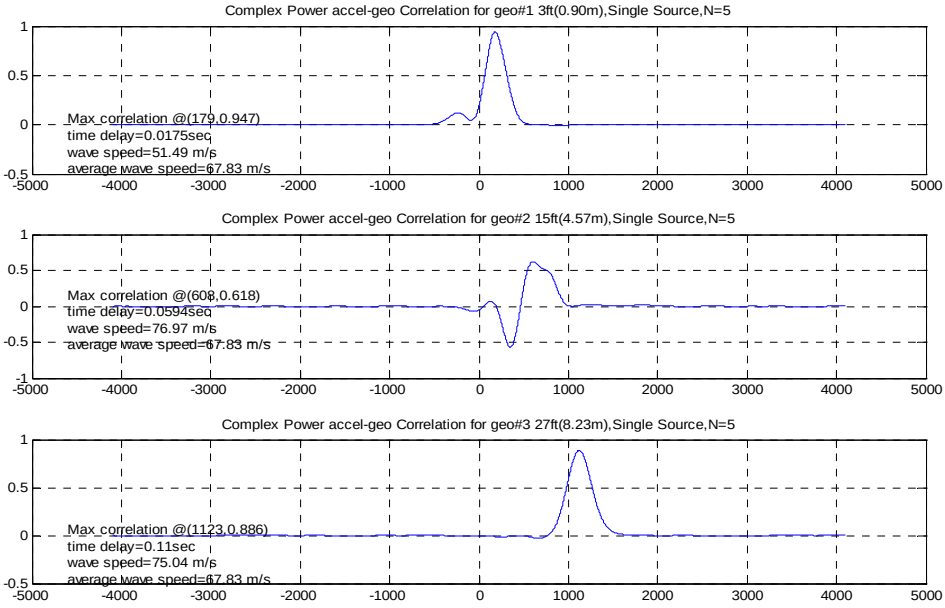


Figure 39. Imaginary Power Wave Speed Calculation Between Accelerometer and Geophones

The results of the wave speed calculations for geophones placed in line were tabulated and shown in Table 4.

| Range (ft) | Radial (m/s) | Vertical (m/s) | Complex PWR (m/s) |
|---|---|---|---|
| 3-15 (geo-geo) | 84.99 | 58.93 | 82.55 |
| 15-27 (geo-geo) | 66.57 | 126.62 | 86.36 |
| 3-27 (geo-geo) | 83.19 | 73.20 | 80.08 |
| 3 (accel-geo) | 60.63 | 76.80 | 51.49 |
| 15 (accel-geo) | 78.92 | 118.77 | 76.97 |
| 27 (accel-geo) | 73.03 | 73.67 | 75.04 |

Table 4. Calculated Wave Speeds for G1, G2 and G3 (100 Hz)

The calculated average wave speed is approximately equal to 80m/s, which is consistent with previous observations and acceptable. Also using the same method with only geophone and accelerometer cross correlation, the average wave speed obtained from G4, G5 and G6 placed in angular separation can be calculated. Table 5 shows the calculated wave speed.

| Geo # | Radial (m/s) | Vertical (m/s) | Complex Power (m/s) |
|---|---|---|---|
| 4 | 90.95 | 109.06 | 66.16 |
| 5 | 121.40 | 54.86 | 90.18 |
| 6 | 93.97 | 121.55 | 93.04 |
| Average | 102.10 | 95.16 | 83.13 |

Table 5. Calculated Wave Speeds for G4, G5 and G6 (100Hz)

The results of wave speed calculations for geophones placed in line and angular positions with G1 at range of 48 feet (14.63m) from the center of the source were tabulated and shown in Table 6 and Table 7.

| Range (ft) | Radial (m/s) | Vertical (m/s) | Complex PWR (m/s) |
|---|---|---|---|
| 48-60 (geo-geo) | 85.57 | 83.47 | 65.18 |
| 60-72 (geo-geo) | 84.41 | 84.03 | 109.59 |
| 48-72 (geo-geo) | 84.70 | 83.66 | 78.41 |
| 48 (accel-geo) | 79.43 | 91.24 | 95.91 |
| 60 (accel-geo) | 84.29 | 85.17 | 81.54 |
| 72 (accel-geo) | 84.18 | 84.95 | 86.78 |

Table 6. Calculated Wave Speeds for G1, G2 and G3 Placed in Line with G1 at range of 48 feet (14.63m) (100 Hz)

| Geo# | Radial (m/s) | Vertical (m/s) | Complex PWR (m/s) |
|---|---|---|---|
| 4 | 95.51 | 102.29 | 101.29 |
| 5 | 84.94 | 95.46 | 96.05 |
| 6 | 80.62 | 77.07 | 93.55 |
| Average | 87.02 | 91.61 | 96.96 |

Table 7. Calculated Wave Speed for G4, G5 and G6 Placed in Angular positions with G6 at range of 60 feet (18.29m) (100 Hz)

### 3. Geophones Placed in Angular Positions

In this field testing, six geophones were first placed in angular positions from 0 to 75 degrees, separated by 15 degrees at a range of approximately 4m. The source was energized and received radial and vertical velocity data wave collected. Once finishing data acquisition for the first quadrant, these six geophones were moved to the next quadrant from 90 to 165, then from 180 to 255, and from 270 to 345 degrees, also separated by 15 degrees again, which gives 24 increments to complete a 360 degree circle. The phase settings were the same as the settings in previous sections. The source was driven with the five-cycle wave packet of 100 Hz, repeated on a time interval of one second.

Again, the synchronous average of 16 successive shots was records. Appendix F shows the calculated wave speed. Figure 40 shows the source and geophone layout as, an example, which was used to measure the beam patterns.

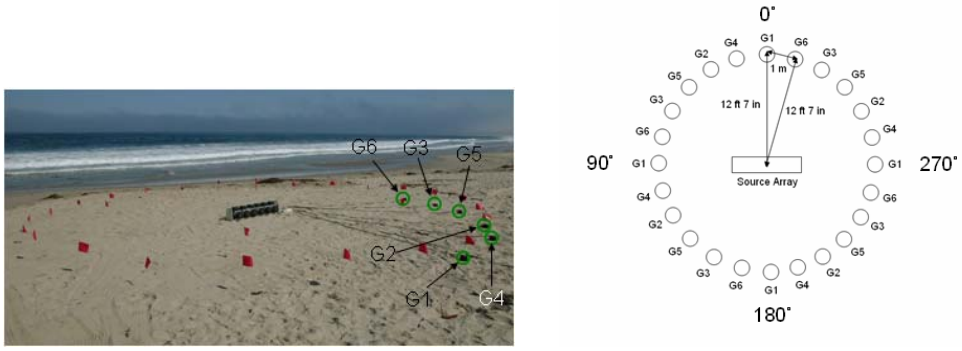


Figure 40. Geophones Placed in Angular Positions (Sep 30 2005)

The distance between adjacent geophones was set to be 1 meter. Therefore, the distance between each geophone and the center of the line source was approximately equal to 3.84 meter. Figure 41 shows the methodology for determining accurate geophone positions.

The distance between the center of the source R can be calculated by using trigonometry,

$$R = \frac{L}{\sin(7.5°)} \cong 3.85m \text{ , where L=0.5m.}$$

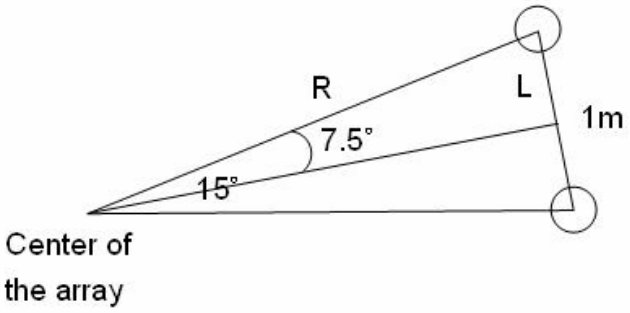


Figure 41. Methodology for Determining the Distance Between Source and Geophone

## F. LINE SOURCE THEORY

In this research, the carrier frequency is set to be 100 Hz; the number of cycles in the wave packet is allowed to be five to have a transient signal. The length of the source is 1.17m; the width of the line source is 0.2m. Based on the past and present experience, the Rayleigh wave speed at the beach site is approximately 90m/s. [Ref.10]

In order to have a theoretical beam pattern to compare to the experimental beam patterns, three theoretical beam patterns calculations were performed. The calculations that were performed do not take into account the elliptical particle motion; they only account for spatial distribution.

A standard continuous-wave far-field beam pattern for a continuous line source was calculated using

$$b_{cw}(\theta) = 20\log\left(\left|\frac{\sin(\nu)}{\nu}\right|\right), \qquad \nu = \frac{kL}{2}\sin(\theta),$$

where $b(\theta)$ is the beam pattern in dB, $k = \frac{2\pi}{\lambda} = \frac{2\pi f}{c}$ is the radian wavenumber and $L$ is the length of the line source. Two transient-wave far-field beam patterns were calculated. First, the range-normalized far-field received transient waveform as a function of angle was calculated by a simple retarded-time superposition integration over the footprint (aperture) of the source, assuming uniform, coherent excitation:

$$s_{rcv}(\mathbf{r}_{rcv}, t) = \iint_{A_{src}} s_{src}(\mathbf{r}_{src}, t - \tau(\mathbf{r}_{src}, \mathbf{r}_{rcv}))dA\,,$$

where $s_{src}$ and $s_{rcv}$ are the signals at the source and receiver points, respectively, and $t = |\mathbf{r}_{src} - \mathbf{r}_{rcv}|/c$ is the propagation time delay between source and receiver. The origin of coordinates was placed at the center of the source aperture, and the average propagation time was taken out, so that the maximum received signal at each angle occurred at $t = 0$. Figure 43 shows representative results.

Two beam patterns were calculated from these results. In one, the beam pattern was calculated from the ratio of the (single-point-in-time) central maximum value of the received signal as a function of time between a point at angle $\theta$ and at 0 degrees using

$$b_{\max}(\theta) = 20\log\left(\frac{s_{rcv}(\theta, t=0)}{s_{rcv}(\theta=0, t=0)}\right).$$

In the other, the beam pattern was calculated from the (central) maximum value of the cross-correlation between the signals received at angles $\theta$ and 0 degrees using

$$b_{xcor}(\theta) = 20\log\left(\frac{xcorr(s_{rcv}(\theta,t), s_{rcv}(\theta=0,t))}{xcorr(s_{rcv}(\theta=0,t), s_{rcv}(\theta=0,t))}\right).$$

Figures 42 and 43 show the results. The green curve in each figure shows $b_{cw}(\theta)$, the red curve shows $b_{max}(\theta)$, and the blue curve shows $b_{xcor}(\theta)$. It can be seen that the model used to calculate the beam pattern has practically no effect on the major lobe; only the amplitude of the secondary lobe, and perhaps the precise locations of the nulls (the angular resolution of the computed beam patterns is not sufficient to draw a definitive conclusion), are sensitive to which model is used. On average, the secondary lobe was 15 dB down compared to the major lobe, with a variation of approximately ±1 dB (approximately 10 percent effect in received signal).

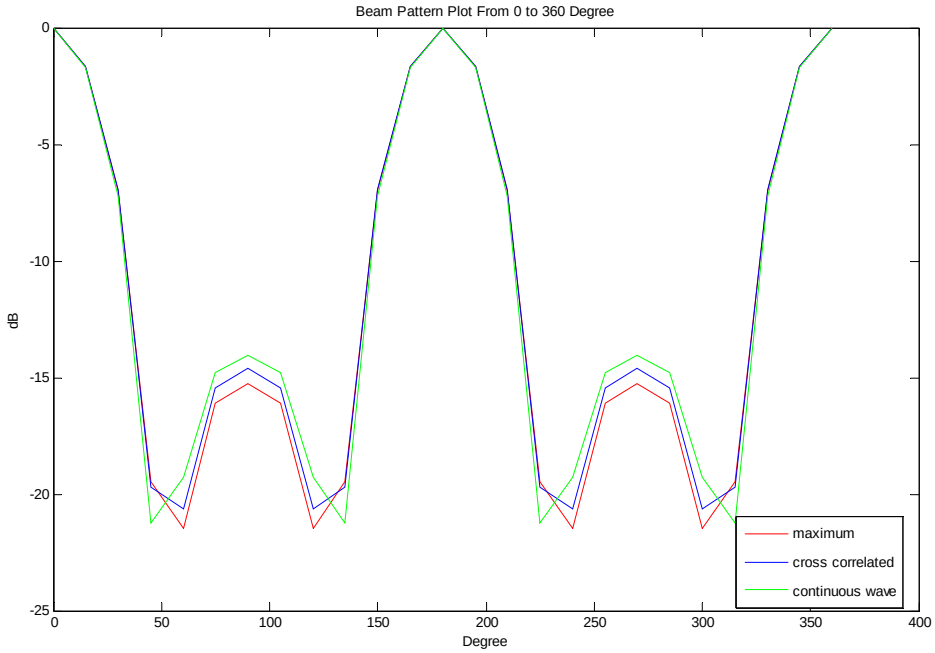


Figure 42. Beam Pattern Plot for Line Source from 0 to 360 Degrees.

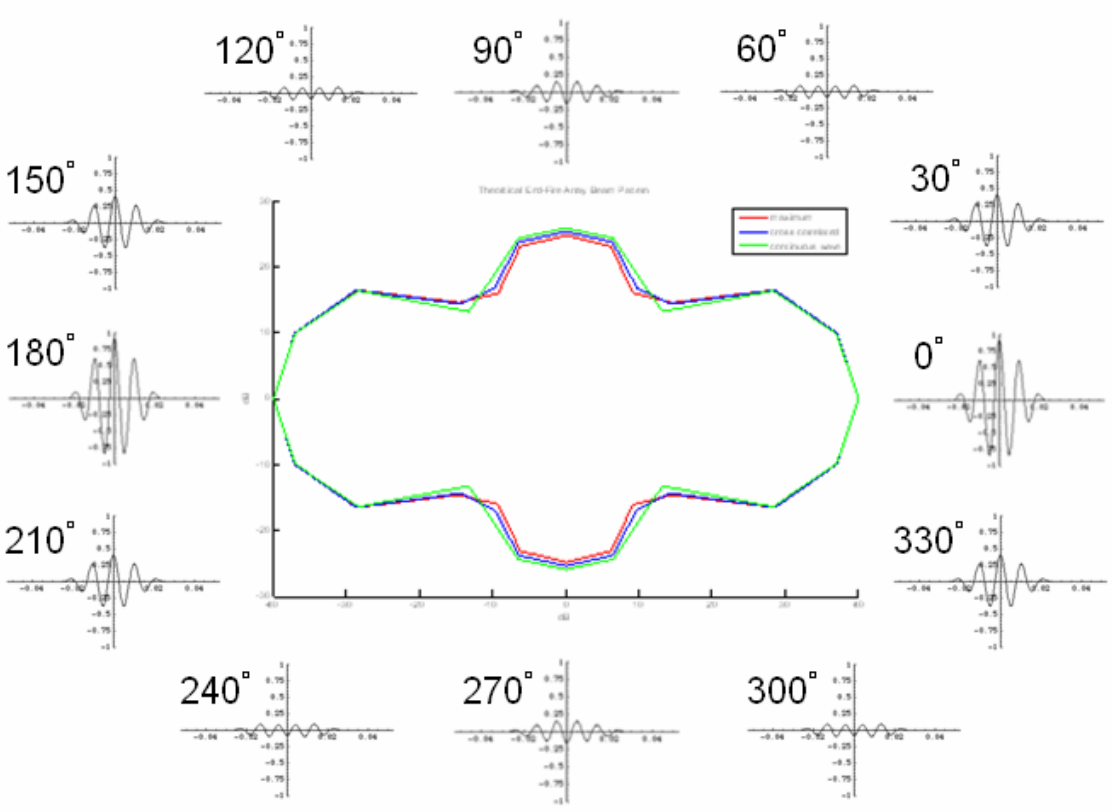


Figure 43. Beam Pattern Polar Plot

## G. LINE SOURCE BEAM PATTERNS

Figures 44, 45, and 46 below show the observed beam patterns using vertical shakers driven only, and for both radial and vertical excitation, with vertical relative phase -90 degrees and +90 degrees, respectively. The experimental beam patterns were calculated by taking the normalized cross correlation with radial, vertical and imaginary power signals, as described in the previous section, using

$$\text{For radial, } rad\_dB = 20\log_{10}(radial\_corrs),$$

$$\text{For vertical, } vert\_dB = 20\log_{10}(vert\_corrs),$$

$$\text{For imaginary power, } imag\_pwr\_dB = 10\log_{10}(imag\_pwr\_corrs).$$

The plots also show the theoretical beam patterns (also see Section V. F).

It should be noted that, because the MATLAB polar plotting command cannot correctly render a beam pattern plot (because of negative dB values), a workaround had to be employed to make the beam pattern plots. First, the value 40 was added to each beam pattern dB value, and the result was then clipped below 0. These values were then passed to the MATLAB polar plotting command. The result is that 40 should be subtracted from the plotted beam pattern dB values (and also the scale values).

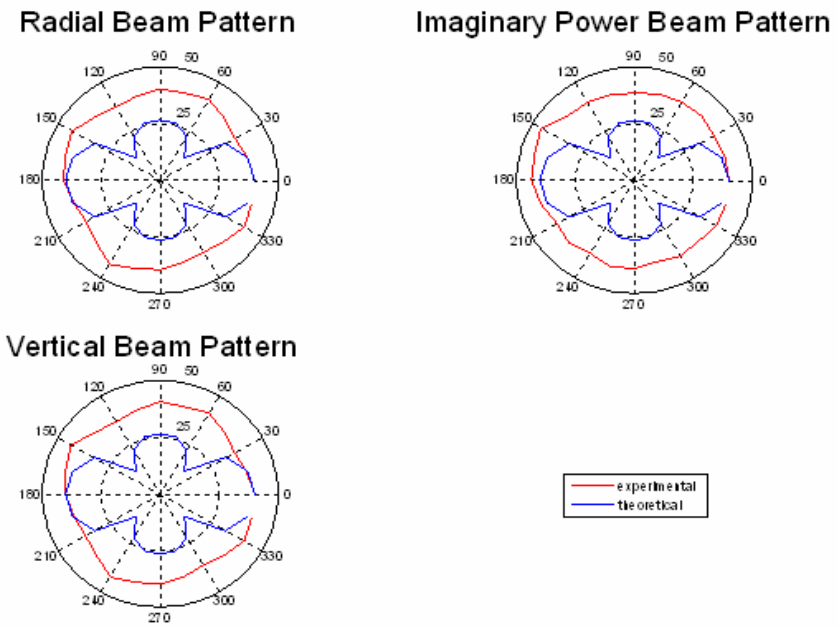


Figure 44. Beam Patterns for Vertical Excitation Only (Sep 30 2005)

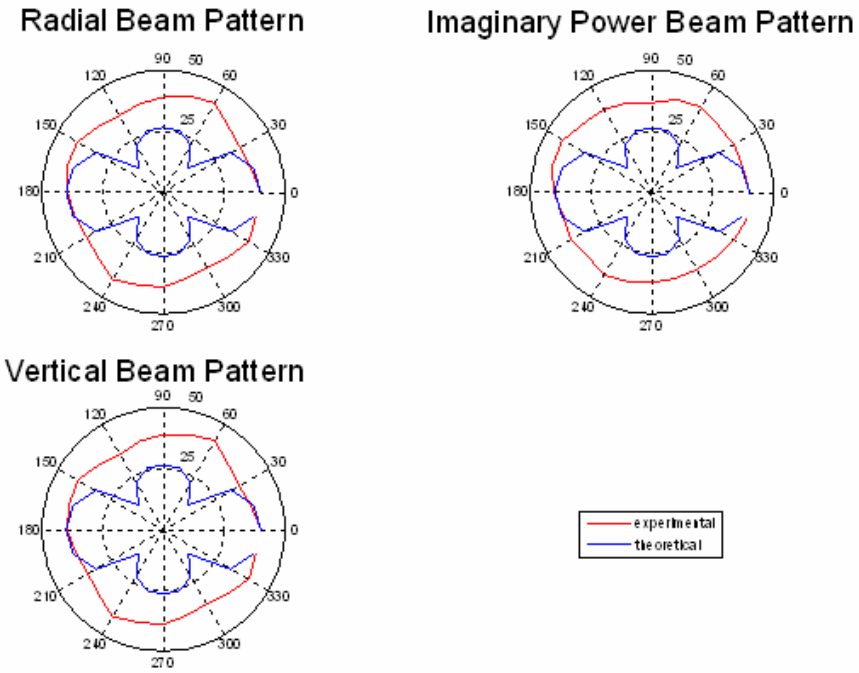


Figure 45. Beam Patterns for Both Radial and Vertical Excitation; Relative Vertical Phase +90 Degrees (Sep 30 2005)

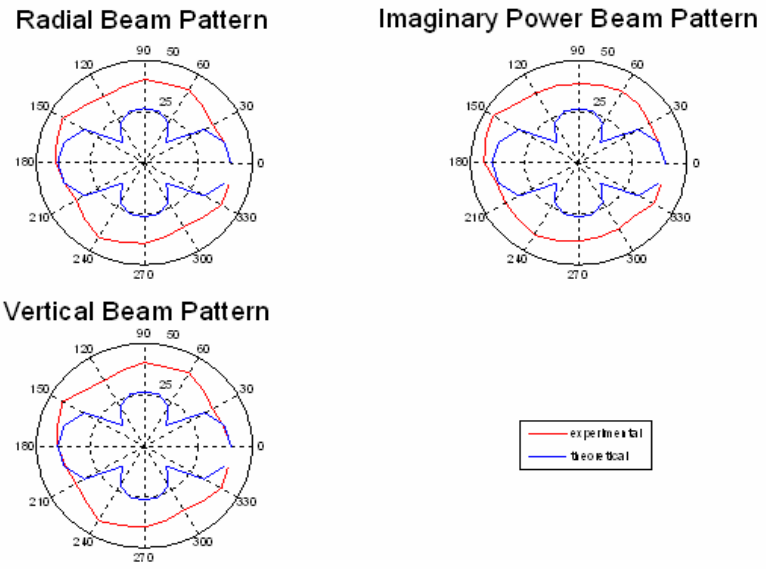


Figure 46. Beam Patterns for Both Radial and Vertical Excitation; Relative Vertical Phase -90 Degrees (Sep 30 2005)

The beam pattern plots above were not consistent with the line source theory. The experimental beam pattern plots did not show the expected directivity property. The reason remains a mystery. One possibility was that the rigid base plate on which the shakers were mounted did not provide adequately uniform coupling to the earth over the aperture footprint of the source. To test this hypothesis, another field test was conducted, with the bottom plate of the source removed and the individual shakers placed in a line on the sand beach. The distance between adjacent shakers was the same as the distance with the bottom plate mounted.

Due to the weather and sea conditions at the testing field, beam pattern measurements were performed only from 0 to 180 degrees. Figure 47 shows the beam pattern plots measured from 0 to 180 degrees. The driven frequency was 100 Hz and only vertical excitation was employed. The experimental result of the beam patterns still didn't show the expected directivity property.

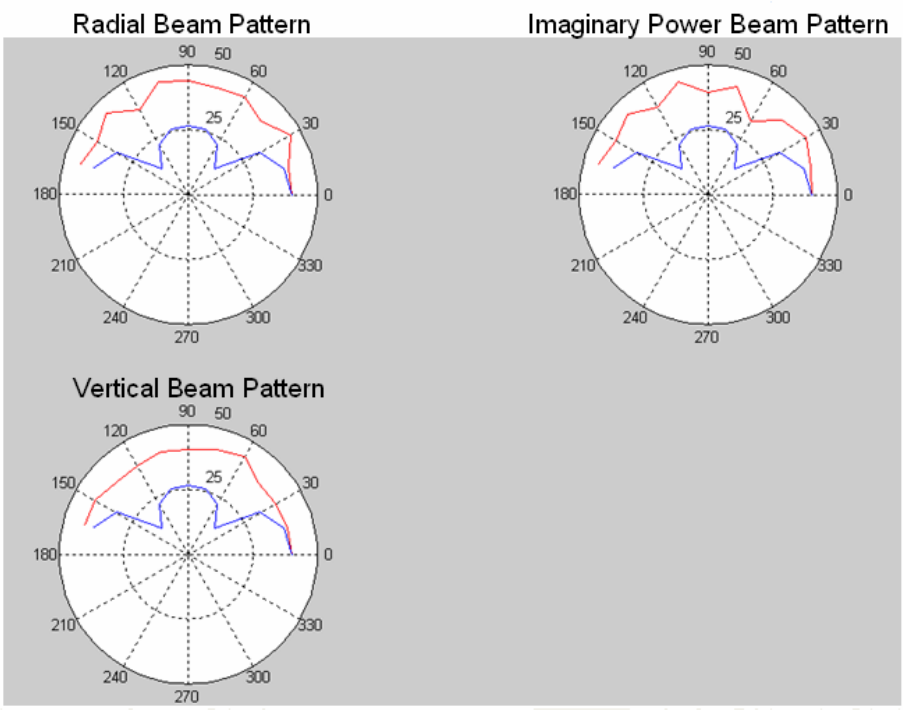


Figure 47. Beam Patterns for Line Array; Vertical Excitation Only (Oct 23 2005)

## H. COMPARISON WITH PREVIOUS RESULTS

The null results of the present investigation are in disappointing contrast to results obtained by several previous NPS students.

In a previous investigation, NPS student Kraig E. Sheetz conducted beam pattern measurements using a line array of seven buried, vertical shakers [Ref. 5]. Figure 48 shows his sources and receivers in the sand beach.

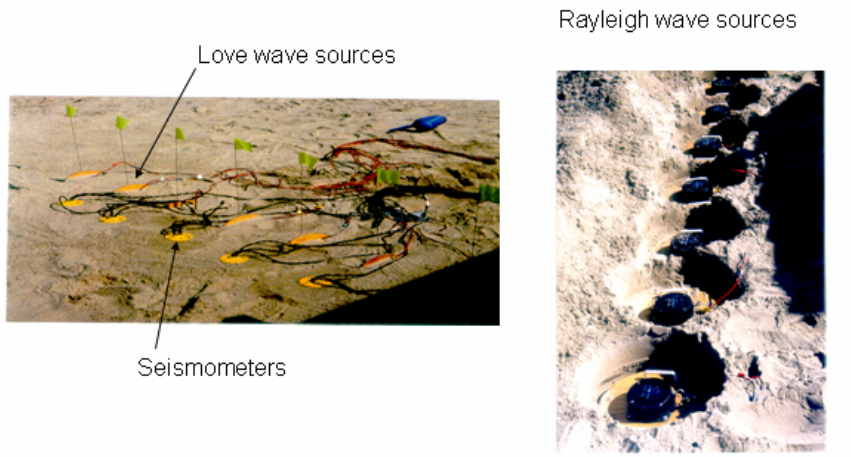


Figure 48. Seven-Element Source Array Experiment

Figure 49 shows his results, which are in fairly good agreement with continuous-wave theory, and certainly show good directivity. However, his sources were buried, and therefore, not mobile.

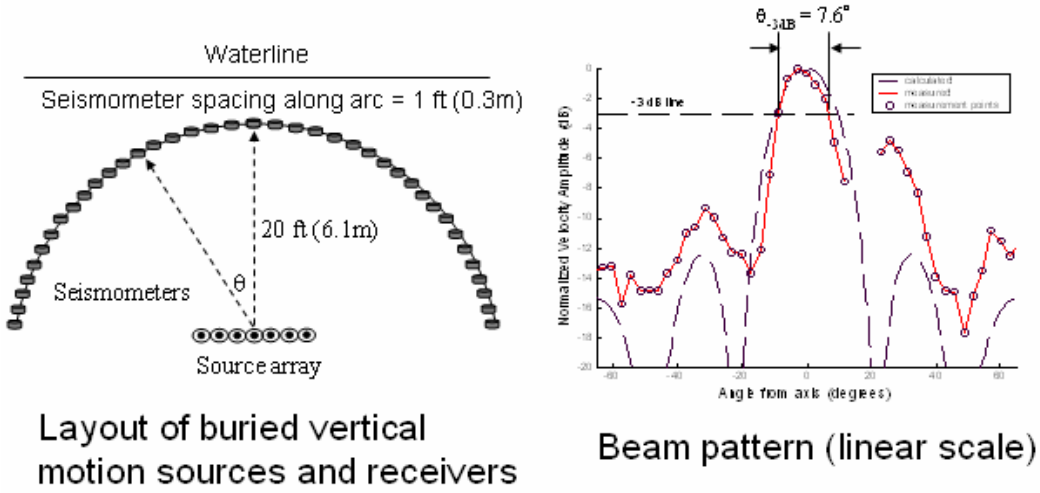


Figure 49. Previous Beam Pattern Experimental Result for Seven-Element Source

In another previous investigation, NPS student Steven E. Rumph measured the transient-wave beam pattern of a 4-element end-fire array of

vertical shakers resting on the sand. Figure 50 shows his experiment at the beach field site. Figure 51 shows his beam pattern results, obtained by cross-correlation. Also shown in Figure 51 is the theoretical continuous-wave beam pattern. It should be noted that the nulls found in the continuous-wave beam pattern cannot be realized with the transient signal Rumph employed. This is illustrated in Figure 52, which shows a model calculation of the ideal transient signal that would be received from Rumph's array (if there were no ringing) and the resulting beam pattern, based on maximum received amplitude. Note the very good similarity of Rumph's measured transient-wave beam pattern and this model calculation. Also, the model calculation predicts a front-to-back reduction of 12 dB. Rumph typically observed a front to back reduction of 10 to 15dB, which is quite consistent with the transient model theory. It is concluded that, with more elements, more front-to-back reduction should be expected. It is recommended that such experiments be undertaken in a further investigation. It is further concluded that, if an end-fire array can be mobilized, it could prove the most effective source for a seismo-acoustic SONAR.

In both Rumph's investigation and in the present investigation, the shaker sources were employed on top of the sand. In Rumph's experiment, however, the geophones (which are the same as employed in the present investigation) were buried flush to the sand surface, versus resting on top. Perhaps this makes a difference; the possibility was not explored. It could also be that the condition of the near-surface region of the beach sand was different, and was not homogeneous enough in the present investigation to support coherent special beamforming.

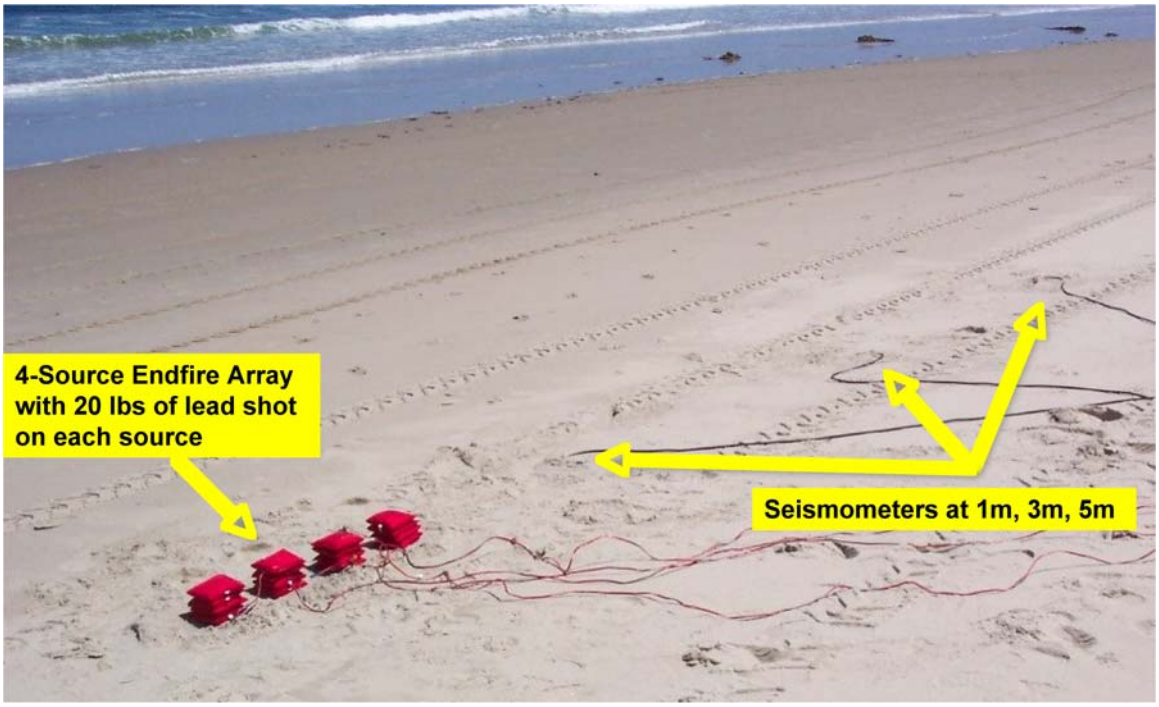


Figure 50. Previous Experiment at the Beach Field Site

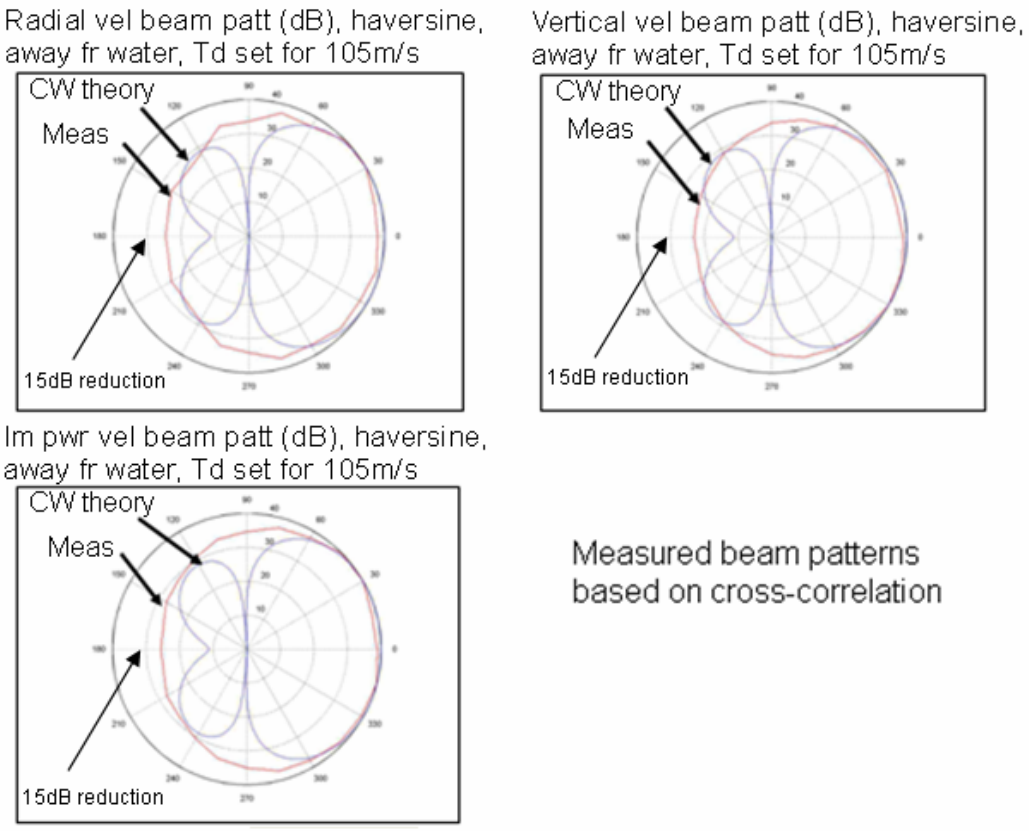


Figure 51. Previous Beam Pattern Experimental Result for End-Fire Source Array

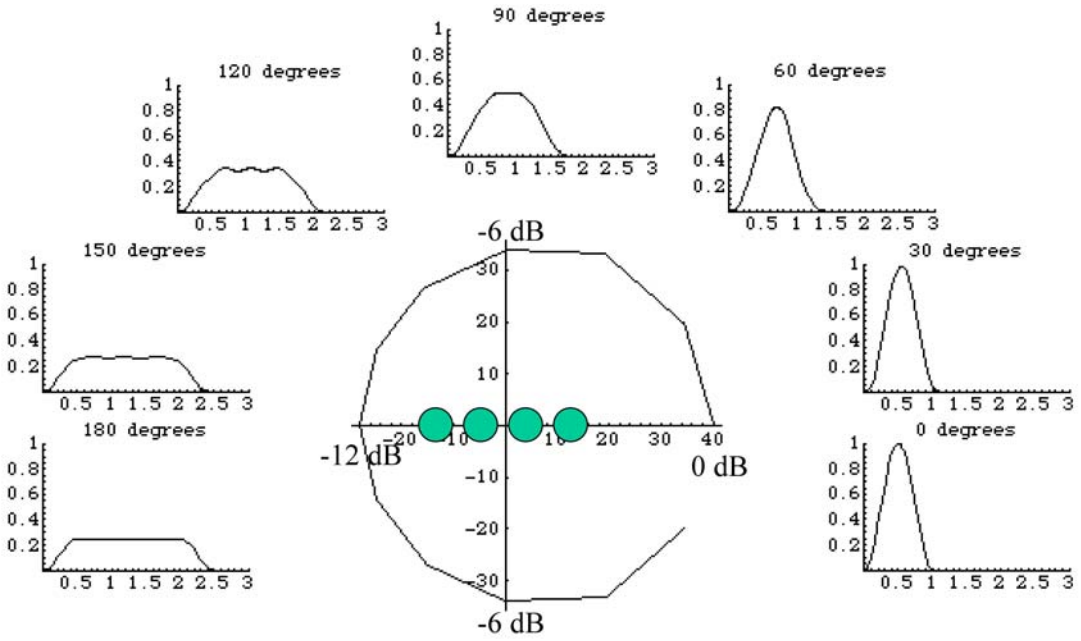


Figure 52. Theoretical Continuous-Wave Beam Pattern

THIS PAGE INTENTIONALLY LEFT BLANK

# VI. CONCLUSION

The goal of the research presented in this thesis was to develop a two-degree-of-freedom, transient-wave, transverse line source to excite Rayleigh waves, which can be used in a seismo-acoustic SONAR to detect buried landmines. The source was composed of six shaker modules mounted on a rigid base plate. Each module contained two horizontal and two vertical inertial mass shakers. All horizontal shakers were driven with a common excitation, as were the vertical shakers. The horizontal and vertical excitations were independent.

Field measurements were conducted at the Del Monte Beach. The source was excited with a 5-cycle amplitude-modulated wave packet, with carrier frequency 100 Hz. Based on past and present observations that the Rayleigh wave speed at the beach test site is about 100 m/s, this results in a Rayleigh wavelength and penetration depth of about one meter. The relative amplitude and phase of vertical and horizontal source excitation were varied to explore their effect on Rayleigh wave generation and source directivity.

Measurements were taken of the radiated vertical and radial velocity at various ranges and angular positions, using geophones resting on the surface. These measurements were used to confirm the production of Rayleigh waves, and to extract their wave speed and the source directional radiation characteristics. The Rayleigh wave speed in this research was found to equal 90 ± 10 m/s, which is consistent with previously observed values. [Ref. 10] A minority number of the wave speed values (see Table 3 and 4) were not consistent with the rest. The reason is unknown.

Unfortunately, none of the observed beam patterns produced by the line source showed any conclusive directivity. Nor did the relative amplitude and phase of source versus vertical excitation make any difference. The reasons for this are unknown. It could be that the near-surface region of the sand medium, wherein the present experiments were conducted, is too inhomogeneous to support coherent special beamforming.

Previous NPS students have investigated the directional radiation characteristics of linear array Rayleigh wave sources, and did observe directivity. One employed buried source elements, which is not suitable for a practical system. The other was a 4-element end-fire array, which employed shakers deployed on the surface. It showed a 10-to-15 dB front-to-back rejection. It is suggested that a larger end-fire array might be the most promising concept for future development into a mobile source for a seismo-acoustic SONAR.

# APPENDIX A. AURA BASS SHAKER SPECIFICATION


**Aura AST-1B-4 (regular, non-pro)**

- Frequency Range: 20-100 Hz
- Effective Impedance: 4 Ohms
- Resonance Frequency (fo): 42 Hz
- Force: 10 LBf (44.5 N) at 25 W
- Peak Force: 20 Lbf (89N) at ??? 50W ???
- Continuous Rated Power: Nominal 25 W RMS
- Max power: 50W RMS
- Resonant Spring: 2 molded nylon/plastic spiders with 3 spokes
- Voice Coil: single layer, 3" diameter, the voice coil is fixed and the magnet is the moving mass in the middle. Xmax ~= Xsus = 1/8".
- Moving Mass: magnet cylinder 3" diameter by 1" height.
- Size: 4.75" (diameter), 2.35" (height)
- Frame Size: 5.4"w x 2.2"h ???
- Weight: 2.5 lbs. (my scale says 2 15/16 pounds)
- Magnet Type: Ceramic
- It is suspected that Aura has dumped this product in favor of the more powerful PRO model.

THIS PAGE INTENTIONALLY LEFT BLANK

# APPENDIX B. SM-11 GEOPHONE SPECIFICATION

SENSOR Nederland bv

## SM-11 Geophone

- 30-Hz geophone with high spurious, over 500 Hz, providing wide bandwidth data suitable for up to 1-ms data sampling
- Can be operated in any orientation
- High output through the use of a special magnet and case design
- Rugged mechanical construction can withstand severe shocks
- 2-year limited warranty

The SM-11 geophone is suitable for use in extended frequency, high-resolution surveys. It has a natural frequency of 30 Hz and a spurious frequency of over 500 Hz, providing a sensor suitable for use with 1-ms sampling recording systems. The use of a special magnetic circuit makes the output of this geophone higher than normal 30-Hz geophones, ensuring adequate signal strength. The high natural frequency spring design also allows this geophone to be used in any orientation (vertical, horizontal, or inverted).

The SM-11 can be installed in the I/O Sensor PE-11 land case.

Typical application: high-resolution seismograph reflection studies.

## Specifications

INPUT/OUTPUT, INC.

| | SM-11/U-FT |
|---|---|
| **Frequency** | |
| Natural frequency ($f_n$) | 30 Hz |
| Tolerance | ±5% |
| Maximum tilt angle for specified $f_n$ | 180° |
| Typical spurious frequency | >500 Hz |
| **Distortion** | |
| Distortion with 0.7 in/s p.p. coil-to-case velocity | <0.2% |
| Distortion measurement frequency | 30 Hz |
| Maximum tilt angle for distortion specification | 180° |
| **Damping** | |
| Open-circuit damping | 0.55 |
| Open-circuit damping tolerance | ±5% |
| **Resistance** | |
| Standard coil resistances | 360 Ω |
| Tolerance | ±5% |
| **Sensitivity** | |
| Open-circuit sensitivity | 30 V/m/s (0.75 V/in/s) |
| Tolerance | ±5% |
| $R_tB_cf_n$ | 7.785 ΩHz |
| Moving mass | 9.2 g (0.32 oz) |
| Maximum coil excursion p.p. | >1 mm (>0.04 in) |
| **Physical Characteristics** | |
| Diameter | 26.6 mm (1.02 in) |
| Height | 32 mm (1.26 in) |
| Weight | 89 g (3.13 oz) |
| Operating temperature range | –40°C to +100°C (–40°F to +212°F) |
| **Limited Warranty Period*** | 2 years |

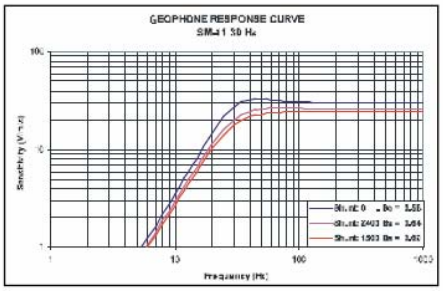


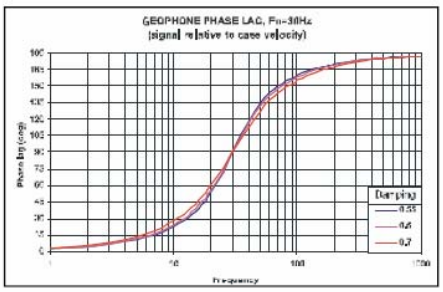


* Warranty excludes damage caused by high-voltage and physical damage to the element case.

All parameters are specified at +20°C in the horizontal position unless otherwise stated.

## Ordering Information

| | |
|---|---|
| **SM-11** | |
| SM-11/U-FT 30 Hz 360 Ω (upright) | P/N 1011010 |
| SM-11/H-FT 30 Hz 360 Ω (horizontal) | P/N 1011030 |


**United States – Stafford, TX**
Input/Output, Inc.
Fax 281.879.3500
Phone 281.933.3339

**England**
Input/Output, Inc.
Fax 44.1603.411403
Phone 44.1603.411400

**Web Site**
www.i-o.com




121024C

# APPENDIX C. ACCELEROMETER SPECIFICATION

PCB PIEZOTRONICS INC.

## Model 354B33

**Product Type:** Accelerometer, Vibration Sensor

Triaxial, thru-hole mounting, quartz shear ICP® accel., 100 mV/g, 1 to 2k Hz, ground isolated, 4-pin conn.

| PERFORMANCE | ENGLISH | SI | |
|---|---|---|---|
| Sensitivity (± 10 %) | 100 mV/g | 10.2 mV/(m/s$^2$) | |
| Measurement Range | ± 50 g pk | ± 490.5 m/s$^2$ pk | |
| Frequency Range (± 5 %) | 1 to 2000 Hz | 1 to 2000 Hz | |
| (± 10 %) | 0.7 to 4000 Hz | 0.7 to 4000 Hz | |
| (± 3 dB) | 0.35 to 6000 Hz | 0.35 to 6000 Hz | |
| Resonant Frequency | ≥ 12 kHz | ≥ 12 kHz | |
| Broadband Resolution | 0.0006 g rms | 0.006 m/s$^2$ rms | [1] |
| Non-Linearity | ≤ 1 % | ≤ 1 % | [2] |
| Transverse Sensitivity | ≤ 5 % | ≤ 5 % | |
| **ENVIRONMENTAL** | | | |
| Overload Limit (Shock) | ± 3000 g pk | ± 29,400 m/s$^2$ pk | |
| Temperature Range | -65 to +250 °F | -54 to +121 °C | |
| Temperature Response | See Graph | See Graph | |
| Base Strain Sensitivity | ≤ 0.02 g/με | ≤ 0.2 (m/s$^2$)/με | [1] |
| **ELECTRICAL** | | | |
| Excitation Voltage | 22 to 30 VDC | 22 to 30 VDC | |
| Constant Current Excitation | 2 to 20 mA | 2 to 20 mA | |
| Output Impedance | ≤ 100 ohm | ≤ 100 ohm | |
| Output Bias Voltage | 10 to 15 VDC | 10 to 15 VDC | |
| Discharge Time Constant | 0.5 to 3.0 sec | 0.5 to 3.0 sec | |
| Settling Time (within 10% of bias) | <20 sec | <20 sec | |
| Spectral Noise (1 Hz) | 270 μg/√Hz | 2646 (μm/s$^2$)/√Hz | [1] |
| (10 Hz) | 70 μg/√Hz | 686 (μm/s$^2$)/√Hz | [1] |
| (100 Hz) | 20 μg/√Hz | 196 (μm/s$^2$)/√Hz | [1] |
| (1 kHz) | 10 μg/√Hz | 98 (μm/s$^2$)/√Hz | [1] |
| Electrical Isolation | >10$^8$ ohm | >10$^8$ ohm | |
| **PHYSICAL** | | | |
| Sensing Element | Quartz | Quartz | |
| Sensing Geometry | Shear | Shear | |
| Housing Material | Titanium | Titanium | |
| Sealing | Hermetic | Hermetic | |
| Size (Height x Length x Width) | 0.44 in x 1.22 in x 0.82 in | 11 mm x 31.0 mm x 20.8 mm | |
| Weight | 0.55 oz | 15.5 gm | [1] |

| | | |
|---|---|---|
| Electrical Connector | 1/4-28 4-Pin | 1/4-28 4-Pin |
| Electrical Connection Position | Side | Side |
| Mounting | Through Hole | Through Hole |
| **SUPPLIED ACCESSORIES:** | | |
| Model 039A23 Allen wrench, 5/32" hex (1) | | |
| Model 081A60 Mounting stud, 10-32 thd, threaded bolt, off ground. (1) | | |
| Model ACS-1T NIST traceable triaxial amplitude response, 10 Hz to upper 5% frequency. (1) | | |
| **OPTIONAL VERSIONS** | | |
| **M** - Metric Mount | | |
| Supplied Accessory : Model M039A23 Allen wrench, 4mm hex (1) replaces Model 039A23 | | |
| Supplied Accessory : Model M081A60 Mounting stud, M5 x 0.80, threaded bolt, off ground. (1) replaces Model 081A60 | | |
| **T** - TEDS Capable of Digital Memory and Communication Compliant with IEEE P1451.4 | | |
| Output Bias Voltage | 10.5 to 16 VDC | 10.5 to 16 VDC |
| Size - Height x Length x Width | 0.44 in x 1.40 in x 1.00 in | 11 mm x 35.6 mm x 25.4 mm |
| Weight | 0.75 oz | 21.3 gm |
| **TLA** - TEDS LMS International - Free Format | | |
| Output Bias Voltage | 10.5 to 16 VDC | 10.5 to 16 VDC |
| Size - Height x Length x Width | 0.44 in x 1.40 in x 1.00 in | 11 mm x 35.6 mm x 25.4 mm |
| Weight | 0.75 oz | 21.3 gm |
| **TLB** - TEDS LMS International - Automotive Format | | |
| Output Bias Voltage | 10.5 to 16 VDC | 10.5 to 16 VDC |
| Size - Height x Length x Width | 0.44 in x 1.40 in x 1.00 in | 11 mm x 35.6 mm x 25.4 mm |
| Weight | 0.75 oz | 21.3 gm |
| **TLC** - TEDS LMS International - Aeronautical Format | | |
| Output Bias Voltage | 10.5 to 16 VDC | 10.5 to 16 VDC |
| Size - Height x Length x Width | 0.44 in x 1.40 in x 1.00 in | 11 mm x 35.6 mm x 25.4 mm |
| Weight | 0.75 oz | 21.3 gm |

***All specifications are at room temperature unless otherwise specified.***

**NOTES:**

[1] Typical.

[2] Zero-based, least-squares, straight line method.

[3] See PCB Declaration of Conformance PS023 for details.

CE [3]

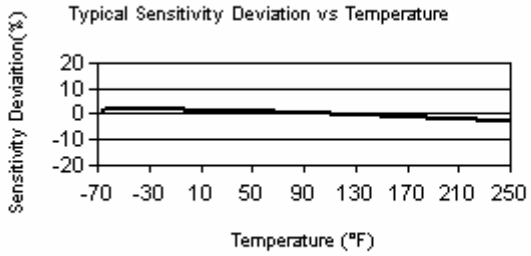


PCB

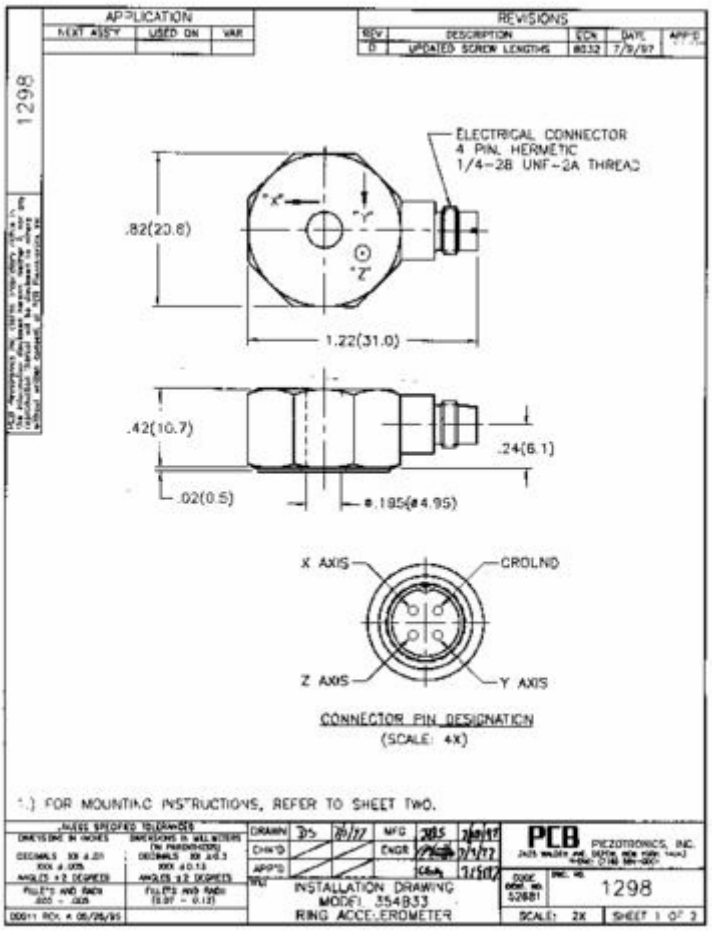
APPLICATION
NEXT ASS'Y
USED ON
VAR
REVISIONS
REV
DESCRIPTION
ECN
DATE
APP'D
D
UPDATED SCREW LENGTHS
8032
7/9/97
1298
ELECTRICAL CONNECTOR
4 PIN, HERMETIC
1/4-28 UNF-2A THREAD
.82(20.8)
"X"
"Y"
"Z"
1.22(31.0)
.42(10.7)
.24(6.1)
.02(0.5)
ø.195(ø4.95)
X AXIS
GROUND
Z AXIS
Y AXIS
CONNECTOR PIN DESIGNATION
(SCALE: 4X)
1.) FOR MOUNTING INSTRUCTIONS, REFER TO SHEET TWO.
UNLESS SPECIFIED TOLERANCES
DIMENSIONS IN INCHES
DECIMALS XX ±.01
XXX ±.005
ANGLES ±2 DEGREES
FILLETS AND RADII
.005 - .025
DIMENSIONS IN MILLIMETERS
(to nearest 0.1)
DECIMALS XX ±0.3
XXX ±0.13
ANGLES ±2 DEGREES
FILLETS AND RADII
(0.127 - 0.13)
DRAWN
DS
10/17
MFG
CHK'D
ENGR
APP'D
MFG
INSTALLATION DRAWING
MODEL 354B33
RING ACCELEROMETER
PCB
PIEZOTRONICS, INC.
DWG. NO.
1298
SCALE: 2X
SHEET 1 OF 2

THIS PAGE INTENTIONALLY LEFT BLANK

# APPENDIX D. SIGNAL ANALYZER SPECIFICATION



## SA390 Specifications

### General

| | |
|---|---|
| Number of Channels | Standard: two (SA610 and SA610DC four channels) |
| | Optional: four, six or eight (SA390DC and SA610DC limited to four channels maximum) |
| Frequency Ranges | dc to 100 kHz full scale in 1, 2, 4, 5 sequence less 50 kHz range, two channels active |
| | dc to 40 kHz full scale 1, 2, 4, 5 sequence, four to eight channels active |
| Anti-Aliasing Filter | Standard on each Channel with 120 dB/Octave rolloff |
| A/D Conversion | Ranges up to 40 kHz: 16 Bit Resolution - All channels parallel sampled |
| | 100 kHz range: 12 Bit Resolution - Two channels parallel sampled |
| Sampling Rate | 2.56 x upper frequency range |
| Maximum Composite Sampling Rate | 819, 200 samples per second |
| DSP Operation | 32 Bit 40 MHz Floating Point Primary Processor (20 Million Floating Point Operations per Second) |
| | 16 Bit Secondary Processor for each channel pair (20 Million Operations per Second) |
| Dynamic Range (analog board type 1) | 0.05 Vrms F.S. to 20.0 Vrms F.S. 0–40 kHz, >90 dB below F.S. with 8 avg. |
| | 40 kHz–100 kHz, >80 dB below F.S. with 8 avg. |
| Noise Floor (analog board type 1) | 0.05 Vrms F.S. to 20.0 Vrms F.S. 0–40 kHz >90 dB below F.S. with 8 avg. |
| | 40 kHz–100 kHz, >80 dB below F.S. with 8 avg. |
| Real Time Performance | >20 kHz real time rate on dual spectrum calculation |
| Full Scale Voltage Range | 0.001 Vrms to 20 Vrms in 1, 2, 5 sequence with autoranging, independently selectable on each channel |

| | |
|---|---|
| Channel to Channel Match (analog board Type 1) | |
| Amplitude: | ± 0.25 dB, 0–40 kHz, 1 mVrms F.S. to 1.0 Vrms F.S. |
| | ± 0.5 dB, 0–40 kHz, 2 Vrms F.S. to 20 Vrms F.S. |
| | ±0.5 dB, 40 kHz–100 kHz, 1 mVrms F.S. to 20 Vrms F.S. |
| Phase: | ± 1.0°, 0–40 kHz, 1 mVrms F.S. to 1.0 Vrms F.S. |
| | ± 3.0°, 0–40 kHz, 2 Vrms F.S. to 20 Vrms F.S. |
| | ±3.0°, 40–100 kHz, 1 mVrms F.S. to 20 Vrms F.S. |
| Cross Talk: | 0.05 Vrms F.S. to 20.0 Vrms F.S. |
| | 0–40 kHz, >85 dB below F.S. with 8 avg. |
| | 40 kHz–100 kHz, >75 dB below F.S. with 8 avg. |
| Input Impedance | 1 MΩ shunted by less than 100 picofarads |
| Input Coupling | dc or ac (-3 dB at 0.5 Hz), selectable each channel |
| Constant Current Power (ICP®) | 4 mA constant current, 24 Vdc maximum, selectable each channel |
| Overload Protection | 100 Vpk input on each channel |
| Triggering | Internally selectable for any channel, single or repeat: |
| | External single or repeat |
| | Slope: Rising or Falling Edge |
| | Delay: Selectable pre- and post- trigger delay in one sample increments |
| Frequency Resolution | 200, 400, 800, or 1600 lines selectable |
| Input Recorder Memory | Standard configuration 7.5 MB distributed between active channels |
| Replay Mode | Auto scan of input recorder memory within user defined boundaries at selected overlap factor |
| | View time record or processed function results |

# APPENDIX E. MATLAB CODE

## A. WAVE SPEED DETERMINATION

```
% This program was written for the data collected on Sep 5, 2005. For other data,
% the distances and frequency must be changed.
% This program uses the geophone placed in line to calculate the wave speed.
% The wave speed can be determined by geophone-to-geophone correlation,
% geophone-to-accelerometer correlation and complex power correlation.
% This program also uses the recorded data to produce Hankel Plots.
clear all
close all
trash=uiimport;
nm=fieldnames(trash);
rawdata=getfield(trash,nm{1});
smoothing=5;
yesorno=input('Make sure you entered the geophone ranges into
r_geo_3ft(0.90m), r_geo_15ft(4.57m), r_geo_27ft(8.23m). (Hit <cr> to continue):')

sample_freq=10240; % Hz
nyq_freq=sample_freq/2;
ctr_freq=100; % Hz
frac_bw=sqrt(2);
[b,a]=butter(1,[ctr_freq/nyq_freq/frac_bw ctr_freq/nyq_freq*frac_bw]);
filtdata=filtfilt(b,a,rawdata);

smoothingstr=int2str(smoothing);
datarange=[1:length(rawdata(:,1))];
geo_1r=filtdata(datarange,1);
geo_1v=filtdata(datarange,2);
geo_2r=filtdata(datarange,3);
geo_2v=filtdata(datarange,6);
geo_3r=filtdata(datarange,5);
geo_3v=filtdata(datarange,4);
accel_r=filtdata(datarange,7);
accel_v=filtdata(datarange,8);
```

```
timeindex=[1:length(geo_1r)];
arrayofones=ones(size(timeindex));
time=timeindex/10.24;   % sample times in msec
%[Y,peakI]=max(sum(xrc390(:,1:6).*xrc390(:,1:6),2));  % find the largest peak of
the data
[Y,peakI]=max(sum(rawdata(datarange,7:8).*rawdata(datarange,7:8),2));
peaktimems=time(peakI);   % peak time in msec

fignum=0;
tmin=peaktimems;
tmax=peaktimems+100;

fignum=fignum+1; figure(fignum)     % figure (1)
subplot(4,1,1)
plot(time,accel_r),title('radial accelerometer output'),grid
subplot(4,1,2)
plot(time,geo_1r),title('radial output at 3 feet(0.9m)'),grid
subplot(4,1,3)
plot(time,geo_2r),title('radial output at 15 feet(4.57m)'),grid
subplot(4,1,4)
plot(time,geo_3r),title('radial output at 27 feet(8.23m)'),grid

fignum=fignum+1; figure(fignum)     % figure (2)
subplot(4,1,1)
plot(time,accel_v),title('vertical accelerometer output'),grid
subplot(4,1,2)
plot(time,geo_1v),title('vertical output at 3 feet(0.9m)'),grid
subplot(4,1,3)
plot(time,geo_2v),title('vertical output at 15 feet(4.57m)'),grid
subplot(4,1,4)
plot(time,geo_3v),title('vertical output at 27 feet(8.23m)'),grid

conv_factor=1/10240;   % sample time in sec

% Ratio of Radial to Vertical Output Plots
fignum=fignum+1; figure(fignum)     % figure (3)
```

```
subplot(4,1,1)
rad_vert_ratio_accel=abs(hilbert(accel_r))./abs(hilbert(accel_v));
plot(time,rad_vert_ratio_accel),title('ratio of radial to vertical accelerometer
output'),grid,axis([-Inf Inf 0 2])
subplot(4,1,2)
rad_vert_ratio1=abs(hilbert(geo_1r))./abs(hilbert(geo_1v));
plot(time,rad_vert_ratio1),title('ratio of radial to vertical output at 3
feet(0.9m)'),grid,axis([-Inf Inf 0 2])
subplot(4,1,3)
rad_vert_ratio2=abs(hilbert(geo_2r))./abs(hilbert(geo_2v));
plot(time,rad_vert_ratio2),title('ratio of radial to vertical output at
15feet(4.57m)'),grid,axis([-Inf Inf 0 2])
subplot(4,1,4)
rad_vert_ratio3=abs(hilbert(geo_3r))./abs(hilbert(geo_3v));
plot(time,rad_vert_ratio3),title('ratio of radial to vertical output at
27feet(8.23m)'),grid,axis([-Inf Inf 0 2])

% Radial geophone-geophone correlations
[geo_12r_corr,lags1r]=xcorr(geo_2r,geo_1r,'coeff');
[peak1r,index1r]=max(geo_12r_corr);
delay1r=conv_factor*lags1r(index1r);
speed1r=3.66/delay1r;   % space between geo #1 and #2 is 12ft(3.66m)
[geo_23r_corr,lags2r]=xcorr(geo_3r,geo_2r,'coeff');
[peak2r,index2r]=max(geo_23r_corr);
delay2r=conv_factor*lags2r(index2r);
speed2r=3.66/delay2r;   % space between geo #2 and #3 is 12ft(3.66m)
[geo_13r_corr,lags3r]=xcorr(geo_3r,geo_1r,'coeff');
[peak3r,index3r]=max(geo_13r_corr);
delay3r=conv_factor*lags3r(index3r);
speed3r=7.32/delay3r;   % space between geo #1 and #3 is 24ft(7.32m)

% Calculation of the average radial speed
speed_ravg=(speed1r+speed2r+speed3r)/3

% Radial geophone-geophone correlation plots which show the calculated wave
speeds
fignum=fignum+1; figure(fignum)     % figure (4)
subplot(3,1,1)
```

```
plot(lags1r,geo_12r_corr),title(['Radial Correlation between 3ft(0.90m) and 15ft(4.57m),Single Source,N=' smoothingstr]),grid

text(-0.45/conv_factor,0*peak1r,sprintf('Max correlation @(%2.0f,%0.3g)\ntime delay=%0.3gsec\nwave speed=%2.2f m/s\naverage radial speed=%2.2f m/s',lags1r(index1r),peak1r,delay1r,speed1r,speed_ravg))

subplot(3,1,2)

plot(lags2r,geo_23r_corr),title(['Radial Correlation between 15ft(4.57m) and 27ft(8.23m),Single Source,N=' smoothingstr]),grid

text(-0.45/conv_factor,0*peak2r,sprintf('Max correlation @(%2.0f,%0.3g)\ntime delay=%0.3gsec\nwave speed=%2.2f m/s\naverage radial speed=%2.2f m/s',lags2r(index2r),peak2r,delay2r,speed2r,speed_ravg))

subplot(3,1,3)

plot(lags3r,geo_13r_corr),title(['Radial Correlation between 3ft(0.90m) and 27ft(8.23m),Single Source,N=' smoothingstr]),grid

text(-0.45/conv_factor,0*peak3r,sprintf('Max correlation @(%2.0f,%0.3g)\ntime delay=%0.3gsec\nwave speed=%2.2f m/s\naverage radial speed=%2.2f m/s',lags3r(index3r),peak3r,delay3r,speed3r,speed_ravg))


% Radial accelerometer-geophone correlations

[ag1r_corr,lagsag1r]=xcorr(geo_1r,accel_r,'coeff');

[peakag1r,indexag1r]=max(ag1r_corr);

delayag1r=conv_factor*lagsag1r(indexag1r);

speedag1r=0.9/delayag1r;    % space to geo #1 is 3ft(0.90m)

[ag2r_corr,lagsag2r]=xcorr(geo_2r,accel_r,'coeff');

[peakag2r,indexag2r]=max(ag2r_corr);

delayag2r=conv_factor*lagsag2r(indexag2r);

speedag2r=4.57/delayag2r;   % space to geo #2 is 15ft(4.57m)

[ag3r_corr,lagsag3r]=xcorr(geo_3r,accel_r,'coeff');

[peakag3r,indexag3r]=max(ag3r_corr);

delayag3r=conv_factor*lagsag3r(indexag3r);

speedag3r=8.23/delayag3r;   % space to geo #3 is 27ft(8.23m)


% Calculation of the average radial speed

speed_agravg=(speedag1r+speedag2r+speedag3r)/3


% Radial accelerometer-geophone correlation plots which show the calculated wave speeds

fignum=fignum+1; figure(fignum)     % figure (5)

subplot(3,1,1)
```

```
plot(lagsag1r,ag1r_corr),title('Radial accel-geo Correlation for geo#1
3ft(0.90m)'),grid
text(-0.45/conv_factor,0*peakag1r,sprintf('Max correlation @(%2.0f,%0.3g)\ntime
delay=%0.3gsec\nwave speed=%2.2f m/s\naverage radial speed=%2.2f
m/s',lagsag1r(indexag1r),peakag1r,delayag1r,speedag1r,speed_agravg))
subplot(3,1,2)
plot(lagsag2r,ag2r_corr),title('Radial accel-geo Correlation for geo#2
15ft(4.57m)'),grid
text(-0.45/conv_factor,0*peakag2r,sprintf('Max correlation @(%2.0f,%0.3g)\ntime
delay=%0.3gsec\nwave speed=%2.2f m/s\naverage radial speed=%2.2f
m/s',lagsag2r(indexag2r),peakag2r,delayag2r,speedag2r,speed_agravg))
subplot(3,1,3)
plot(lagsag3r,ag3r_corr),title('Radial accel-geo Correlation for geo#3
27ft(8.23m)'),grid
text(-0.45/conv_factor,0*peakag3r,sprintf('Max correlation @(%2.0f,%0.3g)\ntime
delay=%0.3gsec\nwave speed=%2.2f m/s\naverage radial speed=%2.2f
m/s',lagsag3r(indexag3r),peakag3r,delayag3r,speedag3r,speed_agravg))


% Vertical geophone-geophone correlations
[geo_12v_corr,lags1v]=xcorr(geo_2v,geo_1v,'coeff');
[peak1v,index1v]=max(geo_12v_corr);
delay1v=conv_factor*lags1v(index1v);
speed1v=3.66/delay1v;   % space between geo #1 and #2 is 12ft(3.66m)
[geo_23v_corr,lags2v]=xcorr(geo_3v,geo_2v,'coeff');
[peak2v,index2v]=max(geo_23v_corr);
delay2v=conv_factor*lags2v(index2v);
speed2v=3.66/delay2v;   % space between geo #2 and #3 is 12ft(3.66m)
[geo_13v_corr,lags3v]=xcorr(geo_3v,geo_1v,'coeff');
[peak3v,index3v]=max(geo_13v_corr);
delay3v=conv_factor*lags3v(index3v);
speed3v=7.32/delay3v;   % space between geo #1 and #3 is 24ft(7.32m)


% Calculation of the average vertical speed
speed_vavg=(speed1v+speed2v+speed3v)/3


% Vertical geophone-geophone correlation plots which show the calculated wave
speeds
fignum=fignum+1; figure(fignum)     % figure (6)
subplot(3,1,1)
```

```
plot(lags1v,geo_12v_corr),title(['Vertical Correlation between 3ft(0.90m) and 15ft(4.57m),Single Source,N=' smoothingstr]),grid

text(-0.45/conv_factor,0*peak1v,sprintf('Max correlation @(%2.0f,%0.3g)\ntime delay=%0.3gsec\nwave speed=%2.2f m/s\naverage vertical speed=%2.2f m/s',lags1v(index1v),peak1v,delay1v,speed1v,speed_vavg))

subplot(3,1,2)

plot(lags2v,geo_23v_corr),title(['Vertical Correlation between 15ft(4.57m) and 27ft(8.23m),Single Source,N=' smoothingstr]),grid

text(-0.45/conv_factor,0*peak2v,sprintf('Max correlation @(%2.0f,%0.3g)\ntime delay=%0.3gsec\nwave speed=%2.2f m/s\naverage vertical speed=%2.2f m/s',lags2v(index2v),peak2v,delay2v,speed2v,speed_vavg))

subplot(3,1,3)

plot(lags3v,geo_13r_corr),title(['Vertical Correlation between 3ft(0.90m) and 27ft(8.23m),Single Source,N=' smoothingstr]),grid

text(-0.45/conv_factor,0*peak3v,sprintf('Max correlation @(%2.0f,%0.3g)\ntime delay=%0.3gsec\nwave speed=%2.2f m/s\naverage vertical speed=%2.2f m/s',lags3v(index3v),peak3v,delay3v,speed3v,speed_vavg))


% Vertical accelerometer-geophone correlations

[ag1v_corr,lagsag1v]=xcorr(geo_1v,accel_v,'coeff');

[peakag1v,indexag1v]=max(ag1v_corr);

delayag1v=conv_factor*lagsag1v(indexag1v);

speedag1v=0.90/delayag1v;   % space to geo #1 is 3ft(0.90m)

[ag2v_corr,lagsag2v]=xcorr(geo_2v,accel_v,'coeff');

[peakag2v,indexag2v]=max(ag2v_corr);

delayag2v=conv_factor*lagsag2v(indexag2v);

speedag2v=4.57/delayag2v;   % space to geo #2 is 15ft(4.57m)

[ag3v_corr,lagsag3v]=xcorr(geo_3v,accel_v,'coeff');

[peakag3v,indexag3v]=max(ag3v_corr);

delayag3v=conv_factor*lagsag3v(indexag3v);

speedag3v=8.23/delayag3v;   % space to geo #3 is 27ft(8.23m)


% Calculation of the average vertical speed

speed_agvavg=(speedag1v+speedag2v+speedag3v)/3


% Vertical accelerometer-geophone correlation plots which show the calculated wave speeds

fignum=fignum+1; figure(fignum)     % figure (7)

subplot(3,1,1)
```

```
plot(lagsag1v,ag1v_corr),title('Vertical accel-geo Correlation for geo#1
3ft(0.90m)'),grid

text(-0.45/conv_factor,0*peakag1v,sprintf('Max correlation @(%2.0f,%0.3g)\ntime
delay=%0.3gsec\nwave speed=%2.2f m/s\naverage radial speed=%2.2f
m/s',lagsag1v(indexag1v),peakag1v,delayag1v,speedag1v,speed_agvavg))

subplot(3,1,2)

plot(lagsag2v,ag2v_corr),title('Vertical accel-geo Correlation for geo#2
15ft(4.57m)'),grid

text(-0.45/conv_factor,0*peakag2v,sprintf('Max correlation @(%2.0f,%0.3g)\ntime
delay=%0.3gsec\nwave speed=%2.2f m/s\naverage radial speed=%2.2f
m/s',lagsag2v(indexag2v),peakag2v,delayag2v,speedag2v,speed_agvavg))

subplot(3,1,3)

plot(lagsag3v,ag3v_corr),title('Vertical accel-geo Correlation for geo#3
27ft(8.23m)'),grid

text(-0.45/conv_factor,0*peakag3v,sprintf('Max correlation @(%2.0f,%0.3g)\ntime
delay=%0.3gsec\nwave speed=%2.2f m/s\naverage radial speed=%2.2f
m/s',lagsag3v(indexag3v),peakag3v,delayag3v,speedag3v,speed_agvavg))


% Hankel Plot

fignum=fignum+1; figure(fignum)     % figure (8)

%velmax=0.03;

thodogram=tmin*arrayofones;

subplot(2,2,1)

plot3(accel_r,time,accel_v,accel_r,thodogram,accel_v),grid,axis ij,axis([-0.03
0.03 10 70 -0.03 0.03])

xlabel('Accel Radial'),ylabel('Time(msec)'),zlabel('Accel Vertical'),title(['Hankel
Plot for accelerometer,Single Source,N=' smoothingstr])

subplot(2,2,2)

plot3(geo_1r,time,geo_1v,geo_1r,thodogram,geo_1v),grid,axis ij,axis([-0.06 0.06
20 60 -0.06 0.06])

xlabel('Radial'),ylabel('Time(msec)'),zlabel('Vertical'),title(['Hankel Plot for geo#1
3ft(0.9m),Single Source,N=' smoothingstr])

subplot(2,2,3)

plot3(geo_2r,time,geo_2v,geo_2r,thodogram,geo_2v),grid,axis ij,axis([-0.01 0.01
50 130 -0.01 0.01])

xlabel('Radial'),ylabel('Time(msec)'),zlabel('Vertical'),title(['Hankel Plot for geo#2
15ft(4.57m),Single Source,N=' smoothingstr])

subplot(2,2,4)

plot3(geo_3r,time,geo_3v,geo_3r,thodogram,geo_3v),grid,axis ij,axis([-0.01 0.01
90 160 -0.01 0.01])

xlabel('Radial'),ylabel('Time(msec)'),zlabel('Vertical'),title(['Hankel Plot for geo#3
27ft(8.23m),Single Source,N=' smoothingstr])
```

```
% Complex Power
complex_accel_r=hilbert(accel_r);
complex_accel_v=hilbert(accel_v);
complex_power_accel=conj(complex_accel_v).*complex_accel_r;
complex_1r=hilbert(geo_1r);
complex_1v=hilbert(geo_1v);
complex_power_1=conj(complex_1v).*complex_1r;
complex_2r=hilbert(geo_2r);
complex_2v=hilbert(geo_2v);
complex_power_2=conj(complex_2v).*complex_2r;
complex_3r=hilbert(geo_3r);
complex_3v=hilbert(geo_3v);
complex_power_3=conj(complex_3v).*complex_3r;

% Imaginary Power Plots
fignum=fignum+1; figure(fignum)     % figure (9)

subplot(4,1,1)
plot(time,imag(complex_power_accel)),title(['Imag Pwr for accelerometer,Single
Source,N=' smoothingstr]),grid    %,axis ([0 2000 min(imag(complex_power_1))
max(imag(complex_power_1))])
xlabel('Time(msec)'),ylabel('Imaginary Part of (complex
conjugate(radial)*complex(vertical))')
subplot(4,1,2)
plot(time,imag(complex_power_1)),title(['Imag Pwr for geo#1 3ft(0.9m),Single
Source,N=' smoothingstr]),grid    %,axis ([0 2000 min(imag(complex_power_1))
max(imag(complex_power_1))])
xlabel('Time(msec)'),ylabel('Imaginary Part of (complex
conjugate(radial)*complex(vertical))')
subplot(4,1,3)
plot(time,imag(complex_power_2)),title(['Imag Pwr for geo#2 15ft(4.57m),Single
Source,N=' smoothingstr]),grid    %,axis ([0 2000 min(imag(complex_power_2))
max(imag(complex_power_2))])
xlabel('Time(msec)'),ylabel('Imaginary Part of (complex
conjugate(radial)*complex(vertical))')
subplot(4,1,4)
plot(time,imag(complex_power_3)),title(['Imag Pwr for geo#3 27ft(8.23m),Single
Source,N=' smoothingstr]),grid    %,axis ([0 2000 min(imag(complex_power_3))
max(imag(complex_power_3))])
```

```
xlabel('Time(msec)'),ylabel('Imaginary Part of (complex
conjugate(radial)*complex(vertical))')


% Imaginary Power goephone-geophone correlations
[power_12_corr,lags1e]=xcorr(imag(complex_power_2),imag(complex_power_1)
,'coeff');
[peak1e,index1e]=max(power_12_corr);
delay1e=conv_factor*lags1e(index1e);
speed1e=3.66/delay1e;        % space between geo#1 and geo#2 is 12ft(3.66m)
[power_23_corr,lags2e]=xcorr(imag(complex_power_3),imag(complex_power_2)
,'coeff');
[peak2e,index2e]=max(power_23_corr);
delay2e=conv_factor*lags2e(index2e);
speed2e=3.66/delay2e;        % space between geo #2 and geo#3 is 12ft(3.66m)
[power_13_corr,lags3e]=xcorr(imag(complex_power_3),imag(complex_power_1)
,'coeff');
[peak3e,index3e]=max(power_13_corr);
delay3e=conv_factor*lags3e(index3e);
speed3e=7.32/delay3e;        % space between geo#1 and geo#3 is 24ft(7.32m)


% Calculation of the average speed
speed_eavg=(speed1e+speed2e+speed3e)/3;


% Imaginary Power goephone-geophone correlation plots which show the
calculated wave speed
fignum=fignum+1; figure(fignum)     % figure (10)
subplot(3,1,1)
plot(lags1e,power_12_corr),title(['Imaginary Power Correlation between geo#1
3ft(0.90m) and geo#2 15ft(4.57m),Single Source,N=' smoothingstr]),grid
text(-0.45/conv_factor,0*peak1e-.2,sprintf('Max correlation
@(%2.0f,%0.3g)\ntime delay=%0.3gsec\nwave speed=%2.2f m/s\naverage wave
speed=%2.2f m/s',lags1e(index1e),peak1e,delay1e,speed1e,speed_eavg))
subplot(3,1,2)
plot(lags2e,power_23_corr),title(['Imaginary Power Correlation between geo#2
15ft(4.57m) and geo#3 27ft(8.23m),Single Source,N=' smoothingstr]),grid
text(-0.45/conv_factor,0*peak2e-.2,sprintf('Max correlation
@(%2.0f,%0.3g)\ntime delay=%0.3gsec\nwave speed=%2.2f m/s\naverage wave
speed=%2.2f m/s',lags2e(index2e),peak2e,delay2e,speed2e,speed_eavg))
subplot(3,1,3)
```

```
plot(lags3e,power_13_corr),title(['Imaginary Power Correlation between geo#1 3ft(0.90m) and geo#3 27ft(8.23m),Single Source,N=' smoothingstr]),grid

text(-0.45/conv_factor,0*peak3e-.2,sprintf('Max correlation @(%2.0f,%0.3g)\ntime delay=%0.3gsec\nwave speed=%2.2f m/s\naverage wave speed=%2.2f m/s',lags3e(index3e),peak3e,delay3e,speed3e,speed_eavg))


% Imaginary Power accelerometer-geophone correlations

[power_1e_corr,lagsag1e]=xcorr(imag(complex_power_1),imag(complex_power_accel),'coeff');

[peakag1e,indexag1e]=max(power_1e_corr);

delayag1e=conv_factor*lagsag1e(indexag1e);

speedag1e=0.9/delayag1e;        % space to geo#1 is 3ft(0.90m)

[power_2e_corr,lagsag2e]=xcorr(imag(complex_power_2),imag(complex_power_accel),'coeff');

[peakag2e,indexag2e]=max(power_2e_corr);

delayag2e=conv_factor*lagsag2e(indexag2e);

speedag2e=4.57/delayag2e;        % space to geo#2 is 15ft(4.57m)

[power_3e_corr,lagsag3e]=xcorr(imag(complex_power_3),imag(complex_power_accel),'coeff');

[peakag3e,indexag3e]=max(power_3e_corr);

delayag3e=conv_factor*lagsag3e(indexag3e);

speedag3e=8.23/delayag3e;        % space to geo#3 is 27ft(8.23m)


% Calculation of the average speed

speed_ageavg=(speedag1e+speedag2e+speedag3e)/3;


% Complex Power accelerometer-geophone correlation plots which show the calculated wave speed

fignum=fignum+1; figure(fignum)     % figure (11)

subplot(3,1,1)

plot(lagsag1e,power_1e_corr),title(['Complex Power accel-geo Correlation for geo#1 3ft(0.90m),Single Source,N=' smoothingstr]),grid

text(-0.45/conv_factor,0*peakag1e-.2,sprintf('Max correlation @(%2.0f,%0.3g)\ntime delay=%0.3gsec\nwave speed=%2.2f m/s\naverage wave speed=%2.2f m/s',lagsag1e(indexag1e),peakag1e,delayag1e,speedag1e,speed_ageavg))

subplot(3,1,2)

plot(lagsag2e,power_2e_corr),title(['Complex Power accel-geo Correlation for geo#2 15ft(4.57m),Single Source,N=' smoothingstr]),grid
```

```
text(-0.45/conv_factor,0*peakag2e-.2,sprintf('Max correlation
@(%2.0f,%0.3g)\ntime delay=%0.3gsec\nwave speed=%2.2f m/s\naverage wave
speed=%2.2f
m/s',lagsag2e(indexag2e),peakag2e,delayag2e,speedag2e,speed_ageavg))

subplot(3,1,3)

plot(lagsag3e,power_3e_corr),title(['Complex Power accel-geo Correlation for
geo#3 27ft(8.23m),Single Source,N=' smoothingstr]),grid

text(-0.45/conv_factor,0*peakag3e-.2,sprintf('Max correlation
@(%2.0f,%0.3g)\ntime delay=%0.3gsec\nwave speed=%2.2f m/s\naverage wave
speed=%2.2f
m/s',lagsag3e(indexag3e),peakag3e,delayag3e,speedag3e,speed_ageavg))
```

## B. LINE SOURCE BEAM PATTERN

```
% This program was written for the data collected on Sep 30, 2005.
% This program uses the geophones placed in angular position to determine the
% beam pattern.
clear all
close all
% the vertical only data set for beam pattern
input('Choose the radial data first then the vertical data. (Hit <cr> to continue):')
trash=uiimport;
nm=fieldnames(trash);
all_raddata=getfield(trash,nm{1});
trash=uiimport;
nm=fieldnames(trash);
all_vertdata=getfield(trash,nm{1});
smoothing=5;
num_cols=24;
dataindex=[1:4096];
angles=[0 15 30 45 60 75 90 105 120 135 150 165 180 195 210 225 240 255
270 285 300 315 330 345];

% Complex Power
cmplx_pwr=conj(hilbert(all_vertdata)).*hilbert(all_raddata);
imag_cmplx_pwr=imag(cmplx_pwr);

% Cross Correlations
radnorm=max(xcorr(abs(hilbert(all_raddata(:,1))),abs(hilbert(all_raddata(:,1)))));
vertnorm=max(xcorr(abs(hilbert(all_vertdata(:,1))),abs(hilbert(all_vertdata(:,1)))));
pwrnorm=max(xcorr(imag_cmplx_pwr(:,1),imag_cmplx_pwr(:,1)));
for ndx=[1:num_cols]
radxcorrs(ndx)=max(xcorr(abs(hilbert(all_raddata(:,1))),abs(hilbert(all_raddata(:,n
dx)))))/radnorm;
vertxcorrs(ndx)=max(xcorr(abs(hilbert(all_vertdata(:,1))),abs(hilbert(all_vertdata(:,
ndx)))))/vertnorm;
pwrxcorrs(ndx)=max(xcorr(imag_cmplx_pwr(:,1),imag_cmplx_pwr(:,ndx)))/pwrnor
m;
end
```

```
% Beam Pattern Plots
rad_dB=max(20*log10(radxcorrs)+40,0);
vert_dB=max(20*log10(vertxcorrs)+40,0);
imag_pwr_dB=max(10*log10(pwrxcorrs)+40,0);
angles_radian=(pi/180)*angles(1:num_cols);
f=100;  % frequency in Hz
c=87;   % average wave speed from imaginary power data in m/s
L=1.17; % length of the source in meter
nu=(2*pi*f/c)*(L/2)*sin(angles_radian+2*pi);
theor_dB=max(20*log10(abs(sin(nu)./nu))+40,0);

figure(1)
subplot(2,2,1)
polar(angles_radian,rad_dB,'r'),axis tight
hold on
polar(angles_radian,theor_dB,'b'),axis tight
hold off
title(['Radial Beam Pattern'])
subplot(2,2,3)
polar(angles_radian,vert_dB,'r'),axis tight
hold on
polar(angles_radian,theor_dB,'b'),axis tight
hold off
title(['Vertical Beam Pattern'])
subplot(2,2,2)
polar(angles_radian,imag_pwr_dB,'r'),axis tight
hold on
polar(angles_radian,theor_dB,'b'),axis tight
hold off
title(['Imaginary Power Beam Pattern'])
```

THIS PAGE INTENTIONALLY LEFT BLANK

# APPENDIX F. CALCULATED WAVE SPEEDS FOR GEOPHONES IN ANGULAR POSITIONS

| Vertical signal only | | Both vertical and radial signal on, Vert. Phase -90/Rad. Phase 0 | |
|---|---|---|---|
| Position | WS (m/s) | Position | WS (m/s) |
| G1, G2, G3 (0,30,60) | 85.80 | G1, G2, G3 (0,30,60) | 87.33 |
| G4,G5, G6 (15,45,75) | 87.24 | G4,G5, G6 (15,45,75) | 84.50 |
| G1, G2, G3 (90,120,150) | 83.04 | G1, G2, G3 (90,120,150) | 84.98 |
| G4,G5, G6 (105,135,165) | 82.91 | G4,G5, G6 (105,135,165) | 87.82 |
| G1, G2, G3 (180,210,240) | 81.09 | G1, G2, G3 (180,210,240) | 80.35 |
| G4,G5, G6 (195,225,255) | 84.07 | G4,G5, G6 (195,225,255) | 84.29 |
| G1, G2, G3 (270,300,330) | 86.36 | G1, G2, G3 (270,300,330) | 135.01 |
| G4,G5, G6 (285,315,345) | 90.26 | G4,G5, G6 (285,315,345) | 133.73 |

| Vertical signal only | | Both vertical and radial signal on, Vert. Phase +90/Rad. Phase 0 | |
|---|---|---|---|
| Position | WS (m/s) | Position | WS (m/s) |
| G1, G2, G3 (0,30,60) | 87.52 | G1, G2, G3 (0,30,60) | 88.47 |
| G4,G5, G6 (15,45,75) | 85.75 | G4,G5, G6 (15,45,75) | 87.54 |
| G1, G2, G3 (90,120,150) | 82.06 | G1, G2, G3 (90,120,150) | -13.56 |
| G4,G5, G6 (105,135,165) | 81.43 | G4,G5, G6 (105,135,165) | 81.15 |
| G1, G2, G3 (180,210,240) | 84.38 | G1, G2, G3 (180,210,240) | 86.55 |
| G4,G5, G6 (195,225,255) | 86.67 | G4,G5, G6 (195,225,255) | 82.37 |
| G1, G2, G3 (270,300,330) | 90.09 | G1, G2, G3 (270,300,330) | 85.91 |
| G4,G5, G6 (285,315,345) | 85.78 | G4,G5, G6 (285,315,345) | 81.13 |

# LIST OF REFERENCES


1. http://en.wikipedia.org/wiki/Landmine#History, December 2005.

2. http://www.ausaid.gov.au/human/landmines.cfm, September 2005.

3. http://www.gati.org.tw/forums/fM/forumM68.htm, September 2005.

4. http://www.engagedpage.com/landmines.html, September 2005.

5. Sheetz, Kraig E., *Advancements In Buried Mine Detection Using Seismic SONAR,* Master's Thesis, Naval Postgraduate School, Monterey, California, December 2000.

6. http://www.cna.com.tw/service/magazine/cns/content_027/27-p24.htm, September 2005.

7. Muir, T.G., Smith, D.E., Wilson, P.S., "Seismo-Acoustic SONAR for Buried Object Detection," Proceedings of the Symposium, *Technology and the Mine Problem,* Naval Postgraduate School, Monterey, California, November 1996.

8. Gaghan, Frederick E., *Discrete Mode Source Development and Testing For New Seismo-Acoustic SONAR*, Master's Thesis, Naval Postgraduate School, Monterey, California, December 1998.

9. Ari Ben-Menaham and Sarva Jit Singh, *Seimic Waves and Sources*, Speinger-Verlag New York Inc., 1981.

10. Rumph, Steven E., *Development of Four –Element End-Fire Array As Seismo-Acoustic SONAR Source*, Master's thesis, Naval Postgraduate School, Monterey, California, September 2003.

11. Fitzpatrick, Sean M., *Source Development for a Seismo-Acoustic SONAR*, Master's Thesis, Naval Postgraduate School, Monterey, California, December 1998.

12. Hall, Patrick W., *Detection and Target-Strength Measurement of Buried Objects Using a Seismo-Acoustic SONAR,* Master's Thesis, Naval Postgraduate School, Monterey, California, December 1998.

13. McClelland, Scott C., *A Rolling Line Source for a Seismic SONAR*, Master's Thesis, Naval Postgraduate School, Monterey, California, June 2002.

13. MacLean, Douglas J., *Mobile Source Development for Seismo-SONAR Based Landmine Detection*, Master's Thesis, Naval Postgraduate School, Monterey, California, June 2003.

# INITIAL DISTRIBUTION LIST

1. Defense Technical Information Center
   Ft. Belvoir, Virginia

2. Dudley Knox Library
   Naval Postgraduate School
   Monterey, California

3. Professor Steven R. Baker, Code PH/Ba
   Department of Physics
   Naval Postgraduate School
   Monterey, California

4. Professor Thomas G. Muir
   Department of Physics and Astronomy
   The University of Mississippi
   University, Mississippi

5. Don Brutzman
   Department of Undersea Warfare
   Naval Postgraduate School
   Monterey, California

6. LT Wang, Shu-Kang
   Naval Postgraduate School
   Monterey, California

7. Dr. Douglas Toderoff
   Office of Naval Research, Code 321W
   Arlington, Virginia

8. Mr. David Pistacchio
   Naval Undersea Warfare Center Division Newport
   Newport, Rhode Island